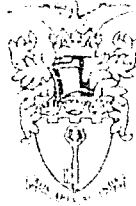


TECH. MEMO
AERO 2147

UNLIMITED

TECH. MEMO
AERO 2147



ROYAL AEROSPACE ESTABLISHMENT

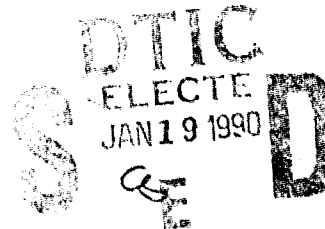
AD-A216 837

A STUDY OF FLOWS OVER HIGHLY-SWEPT WINGS DESIGNED
FOR MANOEUVRE AT SUPERSONIC SPEEDS

by

P. R. Ashill
J. L. Fulker
M. J. Simmons

October 1988



Procurement Executive, Ministry of Defence
Farnborough, Hampshire

9 0 01 18 021

UNLIMITED

BEST
AVAILABLE COPY

G056036

CONDITIONS OF RELEASE

BR-112012

.....

U

COPYRIGHT (c)
1988
CONTROLLER
HMSO LONDON

.....

Y

Reports quoted are not necessarily available to members of the public or to commercial organisations.

UNLIMITED

ROYAL AEROSPACE ESTABLISHMENT

Technical Memorandum Aero 2147

Received for printing 21 October 1988

A STUDY OF FLOWS OVER HIGHLY-SWEPT WINGS DESIGNED
FOR MANOEUVRE AT SUPERSONIC SPEEDS

by

P. R. Ashill

J. L. Fulker

M. J. Simmons

SUMMARY

A wind-tunnel investigation into supersonic free-stream flows over two wing-body configurations, having wings of different design, suitable for combat aircraft, is described. Both wings have the same quasi-delta planform of 60° inboard leading-edge sweep and the same 4% thickness distribution but have differing camber distributions. Following a description of the design of the wings, the test procedures are discussed and the general features of the flows at conditions close to those for sustained manoeuvre are identified and contrasted. Comparisons between calculations by CFD methods and measurement are presented, and it is shown that a multiblock method for solving the Euler equations is suitable for designing wings for efficient manoeuvre at supersonic speeds.

Keywords: Swept wings; Supersonic; Manoeuvrability; Flight manoeuvres; Combat aircraft; Royal Aerospace Establishment

Copyright

©
Controller HMSO London
1988

UNLIMITED

Accession For	
NTIS GRA&I	<input checked="" type="checkbox"/>
DTIC TAB	<input type="checkbox"/>
Unannounced	<input type="checkbox"/>
Justification	
By _____	
Distribution/	
Availability Codes	
Avail and/or	
Special	

A-1

DTIC
 1980
 10/15/80

1 INTRODUCTION

Future combat aircraft will be required to manoeuvre for sustained periods at supersonic speeds. At a typical manoeuvre condition, the lift-dependent drag is a major contribution to aircraft drag, so that measures taken to minimise this drag component may confer combat superiority on the aircraft.

At the high angles of incidence needed for manoeuvre, there may be regions of adverse pressure gradient on the wing, possibly provoking flow separation. Such separations can either be exploited, as with 'vortex flaps', or be eliminated by careful design. In either case, the aim is to maximise the thrust from suction on forward-facing surfaces of the wing and thus to minimise drag.

This paper is concerned with wings designed for attached flow, although the implications for drag of limited regions of separation are considered. Some principles underlying the design of conical wings with attached flow have been described by Miller *et al* (Ref 1) and are illustrated in Fig 1 by sketches of a wing spanwise pressure distribution and conical or 'cross-flow' streamlines, ie the intersections of the stream surfaces with a sphere centred on the wing apex (Ref 2). In the type of flow described by Miller *et al*, the component of free-stream flow normal to the leading edge is subsonic but, at high incidence, the cross flow accelerates around the leading edge to become supercritical on the upper surface. The wing is cambered in the spanwise sense to reduce both the shock strength close to the wing surface (Ref 1) and the penetration of the shock into the flowfield, thereby achieving the dual aim of minimising or eliminating the wave drag due to cross-flow shocks and suppressing the associated separations. Camber also increases the forward-facing area available to provide thrust. Unsustainable suction peaks at the leading edge, both on and off design, are prevented by the use of rounded leading edges.

TM Aero 2147

Although these ideas are applicable to conical wings, they are useful for interpreting flows over lifting wings of quasi-delta planform and with sharp trailing edges, since, as will be seen later, the flows on the upper surface of these wings are of a conical nature.

Since the velocities on the upper surface can be large at manoeuvre conditions, methods based on linearised theory are unsuitable for the design of efficient manoeuvre wings. Methods which solve the exact potential equation are valid for flows with weak shocks and, as such, have been used to design both conical and non-conical wings for shock-free flows on the upper surface (Refs 1 and 3). However, these methods do not represent boundary-layer displacement effects and neglect the increase in entropy through the shock: thus potential-flow methods may be seriously in error when cross-flow shocks of significant strength are present and hence may limit the freedom to make design compromises or to study the effects of departures from the design condition. Methods are available for solving the Euler equations (Refs 4 and 5) which represent the changes in flow quantities across shocks, although, as with the potential-flow methods, they do not represent boundary-layer effects.

Therefore detailed experimental studies are needed of flows over supersonic manoeuvre wings to validate Computational Fluid Dynamic (CFD) methods and to identify flow features not adequately modelled. This paper describes an investigation with these aims, which was performed in the 8ft x 8ft Wind Tunnel, RAE Bedford, on half models of two wing-body configurations, each having the same quasi-delta planform of 60° inboard leading-edge sweep and thickness form of 4% thickness/chord ratio but with differing camber.* The large size of the models enabled them to be manufactured to the desired accuracy and also allowed flow measurements to be made in considerable detail. Manufacturing accuracy is particularly important in the highly-curved region of the leading edge which controls the development of the flow on the upper surface.

After briefly describing the methods used to design the two wings in section 2, the paper continues with a description of the wind-tunnel tests in section 3. A general description of the flows is provided in section 4, and comparisons between predictions by CFD methods and measurement are presented in section 5. Section 5 concludes with an assessment of the drag characteristics of the two wings and considers the implications for the aerodynamic design of wings for supersonic combat aircraft.

2 WING DESIGN

The two wings are illustrated in Fig 2; Wing A has a complex camber surface with camber in both spanwise and streamwise directions while Wing B is of conical camber with the apex at the leading edge of the wing-body junction. The thickness distribution of streamwise sections is a two-parameter type with maximum thickness/chord ratio 4%, as noted before. The other

* Recently, tests were completed on a third member of the family of wings having a symmetrical section. Analysis of these tests is not complete and so no further reference is made to this wing except in section 5 where data from it are used in the analysis of the lift-dependent drag of the other two wings.

parameter was chosen to vary across the wing with the aim of keeping the maximum-thickness locus well swept and having a relatively-large nose radius on the outer wing to avoid large suction peaks there.

Fig 3 shows the spanwise variation of the ratio of the section nose radius r_n to local chord c . Inboard of mid span, the nose-radius ratio is of similar magnitude to those of transonic aerofoils with the same thickness. Further outboard, the nose-radius ratio increases rapidly with spanwise distance, varying between 50% and 80% span in a way similar to the trend for a conical wing for which the leading-edge suction peak is constant across the span (Fig 3).

Also illustrated in Fig 3 is the distribution of nose radius of a delta wing designed by Wood and Bauer (Ref 6). This design has a maximum-thickness locus which is parallel to the leading edge (cf the maximum-thickness locus of the present wing, Fig 3) and uses sections with non-zero base thickness outboard of 66% span to derive a larger nose radius in this region. This spanwise variation of nose radius is similar to that of the present wing. Using a calculation method for solving the full-potential equation, Wood and Bauer found that their wing has lower lift-dependent drag than the corresponding wing with a constant section across the span. They argued that this comes about because the former wing has a larger forward-facing area than the latter for approximately the same conical-type pressure distribution.

Wing A has a camber surface based on that of an earlier design which was studied as part of an extensive programme of research conducted at RAE in the 1950's on slender wings with sharp leading edges suitable for supersonic transport aircraft. Designed using linearised theory, (Ref 7) the original wing was of 71° leading-edge sweep and was cambered so that, at the cruise Mach number 2.2, the leading edge is an attachment line at a lift coefficient $C_L = 0.05$. Chord and span loadings were chosen with the dual aim of achieving low lift-dependent drag and of trimming the aircraft at the cruise lift coefficient 0.1. Wing A retains the spanwise camber distribution of the original wing but with the ordinates scaled to give a leading-edge sweep of 60° . According to the Prandtl-Glauert similarity law this implies that the leading edge of Wing A is an attachment line at $C_L = 0.1$ and at a Mach number of 1.5. This Mach number is typical of supersonic sustained-turn requirements but the lift is about one third of that needed at the tropopause. However, as is shown later, the rounded leading edge ensures that the flow remains attached there for lift coefficients up to and beyond those of interest.

The camber surface of Wing B was designed using the COREL code which solves numerically the exact potential equation for conical flow (Ref 8) and includes an approximate allowance for non-conical effects based on the theory of plane waves (Ref 9). Developed at Grumman Aerospace and made available to RAE by NASA under the terms of an MOD/NASA collaboration, the method is straightforward to use, with a number of useful features for design purposes. In its present form, the method cannot represent a non-conical body, and consequently the 'net-wing' approximation was used (ie the wing plane of symmetry was taken at the body side).

Fig 4 illustrates spanwise pressure distributions calculated by this method for both wings at the axial station $x/c_0 = 0.705$ (as defined in

Fig 5) and for $M = 1.6$. Here the static-pressure coefficient C_p is plotted against spanwise distance from the body centre-line divided by local semi-span, η/A . On the left-hand side of the figure are shown pressure distributions corresponding to the design condition of Wing B, ie at a lift coefficient based on exposed wing area $C_{LE} = 0.4$.

At $x/c_0 = 0.705$, the flow over Wing B at the 'design' condition is predicted to be shock-free on the upper surface while a strong shock is indicated on the upper surface of Wing A. For lower lift coefficients or further upstream, Wing B is predicted to have a re-expansion on the upper surface inboard of the initial compression, followed further inboard by a more severe compression. However, calculations by a three-dimensional boundary-layer method (Ref 10) suggest that separation would be avoided on the upper surface for stations as far aft as $x/c_0 = 0.705$ and for lift coefficients up to 0.4 at $M = 1.6$.

Fig 4 also shows calculated pressure distributions for $C_{LE} = 0.1$ corresponding to that for supersonic dash. In the design of Wing B, special efforts were made to prevent separation on the lower surface at this condition, and, in this respect, Fig 4 shows that the adverse pressure gradients on this surface are smaller on Wing B than on Wing A. The extent to which the design aims of Wing B have been met is discussed in section 4.

3 MODELS AND TEST TECHNIQUES

The layout of both models in the wind tunnel is illustrated in Fig 5; each wing was mounted low on a half body which is cylindrical and nearly rectangular in cross section where the wing intersects the body. Further upstream, the body becomes of circular cross section as the nose is approached.

In each case, the model was attached to a strain-gauge balance outside the working section for the measurement of overall forces. The centre-line of the body was offset approximately 25 mm from the tunnel sidewall to minimise interference between the model and the sidewall boundary layer. Inspection of the wings revealed a high standard of surface finish (0.1-0.2 μm) and that manufacturing errors in the ordinates are small being typically of the order 0.1 mm (0.00006 c_0).

As shown in Fig 5, pressure tappings were provided at nine streamwise stations on each wing and on the side of the body along its centre-line. Model pressures were measured using nine transducers each installed in a 48-way pressure switch and having a working range of ± 1.7 bar. Transducer calibration was effected during each scan, using tunnel total and static pressures as known datum conditions.

The tunnel has good control of stagnation pressure, temperature and humidity down to a frost point of 233 K. The various tunnel and reference pressures were measured by individual self-balancing capsule manometers having highly stable calibrations and zeros. The manometers recording stagnation pressure have a resolution of 0.34 mbar and those monitoring wall static pressures 0.17 mbar. Tunnel total temperature was controlled such that excursions in balance temperature during a test were minimised. This precaution together with corrections to the balance zeros for change

in temperature ensured a high standard of repeatability of balance force measurements. For force and pressure measurement, frost point was maintained below 243 K.

The correction to nominal Mach number was obtained directly from the tunnel calibration and for the conditions studied increases Mach number by 0.005.

In Ref 11 it is shown that measurements of both forces and pressures were made with a high standard of accuracy and repeatability. Measurements of flow pitch angle indicate that the overall error in model incidence is small and probably in the range $\pm 0.02^\circ$.

Boundary-layer transition was fixed by narrow bands of sparsely-distributed ballotini, cemented to the model by epoxy resin. On both surfaces of the wing the band was 25.4 mm from the leading edge in plan view and was 5.08 mm wide. On the body the band was 12.7 mm wide and was located 101.6 mm along the surface downstream of the nose. In all cases, the ballotini were within the range of diameters 0.21-0.25 mm.

Flow visualisations were performed using surface oil flows and vapour screens. The oil was supplied to the upper surface of each wing through holes drilled normal to the surface in three tubes laid across the span (Fig 5). Photographs of the oil flows were taken through a window in the working-section roof to the rear of the model. The vapour screens were illuminated by a vertical fan of laser light produced by reflecting a beam from a 2 W continuous-wave, Argon laser with an oscillating mirror. The streamwise position of the fan could be changed by rotating the mirror about a vertical axis; thus the fan was normal to the tunnel axis at only one streamwise station (see later). The development of the system and the procedures used to obtain satisfactory vapour screens are described in Ref 12. Photographs of the screens were taken by cameras at three positions; (a) in a pod approximately $1.2 c_o$ downstream of the wing trailing edge, (b) in the Schlieren cavity opposite the model and (c) in the working-section roof to the rear of the model. A typical photograph by the camera in the Schlieren cavity is shown in Fig 6. Using arguments put forward convincingly by McGregor (Ref 13), it is possible to identify the main features of the flow from such a vapour screen as indicated in Fig 6.

The tests were performed at a unit Reynolds number of $13.1 \times 10^6/m$ (ie at a Reynolds number based on geometric chord of 12.7×10^6) and for the Mach numbers 1.4, 1.6 and 1.8.

Tests were also made on the body alone for the same range of conditions as the wing-body combinations, with the aim of providing a basis for analysing the overall forces on the wings.

4 GENERAL DESCRIPTION OF FLOWS

This section describes and contrasts the flows over the two wings using measurements of wing pressures and flow visualisations. The discussion is confined to $M = 1.6$, since the flows observed at this Mach number are similar in character to those found at the other Mach numbers studied.

4.1 Wing A

Fig 7 illustrates wing pressure distributions at $M = 1.6$ for a number of incidences, α , and at $x/c_o = 0.705$. Close to zero lift there is a pronounced suction peak near the leading edge on the lower surface. As incidence increases, this peak diminishes - presumably because the attachment line moves from the upper to the lower surface - and the suction on the upper surface increases. The upper-surface suction increases gradually with distance from the leading edge until pressure recovery begins at between 70 and 80% span, the pressure recovery being effected partly by a shock for incidences above about 5° . At all incidences, the pressure distributions suggest that the flow is attached outboard of the shock on the upper surface. However, at lift coefficients above about 0.2, separation occurs at the foot of the shock as indicated by the characteristic bulge in the pressure distribution.

Figs 8, 9 and 10 illustrate isobar patterns on the upper surface (plotted at intervals of 0.05 in C_p unless otherwise indicated) along with sketches from photographs of oil-filament flows and vapour screens for $\alpha = 5.3^\circ$ ($C_L = 0.2$), 7.8° ($C_L = 0.3$) and 10.3° ($C_L = 0.4$). As noted in the Introduction, these flows are of conical character, eg the upper-surface shock is closely aligned with a generator of the 'gross' wing except within the aft 20% chord at the two highest incidences.

In the vapour screens of Figs 8 to 10 and in subsequent figures, the bow wave is indicated by a line outboard of the wing and roughly normal to the edges of the laser fan.

At $\alpha = 5.3^\circ$ the isobars outboard of the shock are generally well swept and there is no evidence in the flow visualisations of leading-edge separation. A shock above the upper surface is indicated by the pronounced turning of the oil filaments, the concentration of isobars and the lines roughly normal to the wing surface in the vapour screens at approximately 70% span. Shock-induced separation is less certain, although a thin dark region in the vapour screen just above the wing suggests that this is a possibility.

At $\alpha = 7.8^\circ$, ($C_L = 0.3$) the isobars near the leading edge converge with increasing axial distance. However, the vapour screens do not point to leading-edge separation anywhere on the wing. The deflection of the oil filaments through the shock is greater than at $\alpha = 5.3^\circ$, and a definite indication of shock-induced separation is provided by the outboard deflection of the oil filaments inboard of the shock. This inference is confirmed by the vapour screens which each reveal a dark bulbous region inboard of the shock indicative of a separation bubble. For stations aft of about 60% chord, the termination of this separation or 'reattachment' is indicated by the clustering together of isobars at about 50% span. A smaller dark region in the vapour screens inboard of the main separation appears to have its origin at the junction of the wing leading-edge and the body, suggesting that this is a separation resulting from wing-body interference. However, this feature does not have a significant effect on wing pressures. The vapour screens also show that, at a given axial station and just above the wing, the inclination of the shock with respect to the wing surface is smaller at $\alpha = 7.8^\circ$ than at $\alpha = 5.3^\circ$. Furthermore, the deflection of the flow normal to the wing surface as it passes through the shock increases noticeably with increase in incidence. The theory of oblique

shocks (Ref 14) shows that these observations are consistent with the shock at $\alpha = 7.8^\circ$ being stronger than that for $\alpha = 5.3^\circ$ as would be expected.

The loss in isobar sweep near the leading edge aft of 80% chord is particularly pronounced at $\alpha = 10.3^\circ$ ($C_L = 0.4$) but again there is no sign of leading-edge separation. A further reduction in shock inclination just above the wing is seen in the vapour screens along with an increase in both the deflection of the flow normal to the wing surface after passing through the shock and the cross-sectional area of the separation. In addition, a second limb is apparent in the shock above the main separation region in the furthest-aft vapour screen, and, in all the vapour screens, dark patches are evident just above the inboard extremity of the main separation indicating regions of re-expansion followed by weak shocks. The concentration of isobars inboard of the shock, symptomatic of reattachment, extends further forward than for $\alpha = 7.8^\circ$.

Near the intersection of the upper-surface shock with the trailing edge, the oil filaments show that the surface flow has a pronounced spanwise component. This effect is probably due to the combined influence of the trailing-edge and upper surface shocks on the boundary layer.

The features noted above become more obvious with further increase of incidence and at values of incidence greater than about 12° the main separation clearly becomes detached from the wing surface and appears to be of the vortex-sheet type.

4.2 Wing B

Fig 11, which corresponds to Fig 5 for Wing A, illustrates the main features of the pressure distributions of Wing B at $x/c_o = 0.705$. As with Wing A, a suction peak is evident near the leading edge on the lower surface at low lift. However, as intended, this peak is of lower magnitude than that of the corresponding peak on Wing A. This aspect is considered again in section 5.

The upper-surface pressure distributions of Wing B also differ in character from those of Wing A. By design, Wing B has higher suction on the outboard 5-10% span than does Wing A, with some isentropic recompression evident at the three largest incidences. Since these suction act on a forward-facing surface, they are a desirable feature of the design of Wing B. However, an unintended re-expansion occurs further inboard leading to a shock forming for $\alpha = 5.4^\circ$ and higher incidences. Reasons for this are discussed in section 5.

Figs 12, 13 and 14 show isobars and flow visualisations for $\alpha = 5.4^\circ$, 7.5° and 10° ($C_L = 0.2, 0.3$ and 0.4). As with Wing A, the upper-surface flows have conical features but, in this case, the upper-surface shock lies close to a generator of the 'net' wing. The flow visualisations of the two wings are broadly similar; however, Wing B does not exhibit the dark patch inboard of the main separation noticed in the vapour screens of Wing A and, furthermore, Wing B is less affected by separation than Wing A, as may be seen by comparing Fig 9 with Fig 13 and Fig 10 with Fig 14. These comparisons reveal that (a) the shock-induced separation bubble of Wing A is bluffer than that of Wing B and (b) the inclination of the upper-surface shock to the wing surface is smaller for Wing A than for Wing B, in both cases for a given axial position and lift coefficient. The lower shock

TN Aero 2147

inclination of Wing A compared to that of Wing B is consistent with the former wing having a stronger upper-surface shock than the latter and this is confirmed by calculations of shock strength from the measured pressure distributions to be described below.

Comparison between Figs 9 and 14 shows that Wing B has roughly the same size and shape of upper-surface separation at $C_L = 0.4$ as Wing A has at $C_L = 0.3$. A more precise indication of the relative significance of the separations of the two wings may be obtained by studying separation 'bluffness', as shown by the vapour screens. Bluffness, defined as the ratio of maximum bubble height relative to the wing surface, h , to bubble width l , is a useful measure of the effect that the separation has on wing pressures. Fig 15 shows values of separation bluffness inferred from the vapour screen labelled $x/c_o = 0.789$ (Fig 14) for a range of angles of incidence. The plots of this ratio against C_L show that Wing B has a lift coefficient of about 0.08 higher than that of Wing A for a given value of h/l , confirming the remark above. Plotted in the same figure against M_N (the Mach number of the flow just upstream of and normal to the locus of the shock on the wing surface, inferred from the measured pressure distributions by simple sweep theory on the assumption that the entropy rise through the bow shock can be ignored) the values of the ratio h/l for the two wings appear to collapse onto a single curve, intersecting the abscissa at $M_N = 1.3$. In other words, shock-induced separation is only significant for values of $M_N > 1.3$.

In one small part of the flow, Wing B shows a stronger viscous-inviscid interaction than does Wing A: this area is close to the intersection of the upper-surface shock with the trailing edge. The oil flows of Figs 9 and 13 reveal that the spanwise flow in this area is greater for Wing B than for Wing A. It is suggested that this difference is due to the trailing-edge shock of Wing B being stronger than that of Wing A, an assertion supported by the measurements of pressures near the trailing edges of the two wings.

5 COMPARISONS BETWEEN CFD METHODS AND MEASUREMENT

In this section, comparisons are presented between predictions by CFD methods and measurement and the drag characteristics of the two wings are assessed. The methods are COREL, already referred to in section 3, and the Euler-Multiblock code, referred to below as EM for brevity. EM was developed jointly by Aircraft Research Association, Bedford (Ref 5) and British Aerospace, Filton (Ref 15) and is based on the finite-volume method for solving the Euler equations of Jameson *et al* (Ref 4).

Boundary-layer effects are not represented in either COREL or EM. However, since the flows considered are supersonic, boundary-layer effects are expected to be important only in the region of the shock.

As noted in section 3, there is no provision in COREL to represent a non-conical body and, because of this, Wing B was designed using the 'net-wing' approximation. Figs 16 and 17 show comparisons of calculations by this method and measurement for Wing B at $M = 1.6$ and $\alpha = 5.4^\circ$ and 7.5° (corresponding to measured overall-lift coefficients of 0.2 and 0.3). These figures suggest that the 'net-wing' approximation is misleading in the way that it fails to represent adequately the re-expansion of the flow

on the upper surface. Some improvement in agreement between COREL and measurement is obtained if the 'gross-wing' approximation is used (ie the wing is extended within the body). Therefore, in any future use of wing-alone methods to design highly-swept wings for supersonic manoeuvre, it is recommended that the 'gross-wing' approximation be used.

A further development of COREL in which the non-conical potential equation is solved, NCOREL, (Ref 16) enables the flow over wing-body combinations to be calculated. Computations by this code of flows over Wing A (with the body represented) have been made by NASA, and comparisons between prediction and measurement are presented in Ref 17. These predictions are comparable in accuracy to those by EM given here.

The topology used in the calculations by EM described in this paper has 'C' and 'H' structures wrapped around streamwise and spanwise sections of the configuration, respectively, and an 'O' structure around the body cross-section. The number of blocks used is 42, and there are 702 cells on each exposed surface of the wing. All the solutions are numerically well-converged, and in Ref 11 it is shown that results for wing pressure distributions are not sensitive to either grid topology or density except possibly close to the wing leading edge.

EM predictions and measurement of spanwise pressure distributions for Wing A are shown in Fig 18a-d for $M = 1.6$ and $\alpha = 0.29^\circ, 3.31^\circ, 5.32^\circ$ and 7.80° corresponding to measured values of $C_L = 0, 0.1, 0.2$ and 0.3 . At low lift, $C_L = 0$, (Fig 18a) EM underestimates the suction peak on the lower surface except at $x/c_o = 0.874$ where the suction peak in the measurement appears to have collapsed, perhaps owing to flow separation. At higher lift, $C_L = 0.1$ and 0.2 , EM gives reasonable predictions of the pressures except at $C_L = 0.2$ inboard of the shock on the upper surface where the calculation method overestimates the suctions. This tendency is more obvious at $C_L = 0.3$ where shock-induced separation is evident. Undulations in the calculated pressure distributions inboard of the shock are attributed to discretisation errors in EM.

Corresponding comparisons are shown in Fig 19a-d for Wing B and indicate that EM predicts the pressure distributions of this wing reasonably well except close to the upper-surface shock. The pressure distributions of Wing A differ significantly from those of Wing B, as noted above, and, in both cases, EM predicts the pressure distributions with reasonable accuracy. This observation, combined with a knowledge of critical conditions for shock-induced separation discussed in section 4, points to the use of EM as a design tool. A successful aspect of the design of Wing B in avoiding separation on the lower surface at low lift is illustrated by the relatively good agreement between calculation and measurement for the pressures on this surface in Fig 19a.

Comparisons between predicted and measured overall forces and pitching moment are described in Ref 11. In this analysis, forces and pitching moment on the body alone are subtracted from those of the wing-body combination at each angle of incidence, thus removing extraneous effects such as those due to the boundary-layer diverter between the body and the tunnel sidewall. The results of this procedure are called notional wing-alone forces. An analogous procedure is used in the calculations by EM, along with the approximation (of slender-body theory) that the forces on the

cylindrical part of the body alone may be ignored. Generally, the agreement between calculation and measurement of lift is reasonable except for flows with shock-induced separation for which EM overestimates the lift at a given incidence. As already shown, this discrepancy arises because, for such flows, the predicted level of suction on the upper surface inboard of the shock are higher than those measured. At low lift ($C_L < 0.1$), EM underestimates drag coefficient by about 0.001, possibly because of the failure of the method to resolve sufficiently accurately the suction peaks on the lower surface* or, in the case of Wing A, because of lower-surface separation. Pitching moment is not predicted accurately, perhaps because of the known sensitivity of pitching moment to errors in wing pressures and also because of the neglect in the calculation method of forces on the cylindrical part of the isolated body. However, the difference in zero-lift pitching moment coefficient (based on geometric mean chord) between the two wings (A-B) is estimated with reasonable accuracy, the value from experiment being $\Delta C_{M_0} = 0.0165$ and by calculation 0.0145. This level of accuracy should be adequate for the assessment of the relative trim drags of different wings.

Fig 20, taken from Ref 11, shows differences in drag and axial force between the two wings, the suffix w referring to notional wing-alone forces. At low lift ($C_L = C_{Lw} < 0.1$), the predictions of drag difference are in reasonable accord with measurement (Fig 21a). However, at values of C_{Lw} above 0.2, the measured difference increases relative to the predicted values. Fig 21b reveals that the trend of ΔC_{Aw} with C_{Lw} is similar to that measured, implying that the discrepancy in drag difference is due to errors in the estimated incidence at a given lift. As noted earlier, the calculation method overestimates lift at a given incidence for flows with shock-induced separation, and Wing B is less prone to shock-induced separation than Wing A. Hence there appears to be a link between the larger drag difference of the measurement compared with that of calculation and shock-induced separation. Therefore it is reasonable to infer that shock-induced separation should be prevented if the aim is to minimise drag. It will be recalled from section 4 that this is achieved if the Mach number of flow just upstream of and normal to the shock is less than about 1.3.

Finally, Fig 21, shows the result of an analysis of the lift-dependent drag of the two wings derived from the experimental results. The data are presented in the form of a figure of merit λ , the ratio of the lift-dependent drag** of the notional wing alone to that of linear theory.*** The calculations by linear theory are made for a flat wing of cropped delta planform (Ref 18), approximating to the planform of the present wings, as shown in Fig 21. Consistent with the definition of notional wing-alone

* In the calculations, drag is determined by integrating the streamwise components of pressures around the wing and combining this with an estimated skin-friction drag. The calculated drag is therefore sensitive to errors in pressure, particularly near the leading edge.

** The zero-lift drag used to calculate lift-dependent drag was determined from the tests on the third, symmetrical wing of the family of wings.

*** The ratio λ may be considered to be a figure of merit since, in the linear theory approximation, effects which reduce the thrust forces on the wing (eg upper-surface shock waves) are absent.

REF 18

forces, only forces on the part of the wing aft of the junction of the wing leading-edge and the body are considered in the linear-theory calculations. Also shown in Fig 21 is a curve derived from information in Ref 6 illustrating a 'practical goal' for the ratio λ . As might be expected from Fig 20, Wing B is superior to Wing A insofar as the former wing yields lower values of λ than the latter. However, for values of C_{LW} greater than about 0.14, Wing B also has a higher lift-dependent drag than that suggested as a practical goal. For values of C_{LW} greater than about 0.25 this can be explained in part by the appearance of shock-induced separation while for $0.15 < C_{LW} < 0.25$ the extra wave drag due to upper-surface shocks would appear to be the sole cause. According to an unpublished theoretical study by Miss C.J. Betts (RAE Bedford) of wave drag of conical wings of differing camber and thickness, wave drag due to upper-surface shocks is significant only for values of M_N greater than 1.2. Calculations, based on measured pressure distributions, indicate that M_N is greater than 1.2 for stations aft of 50% chord on Wing B for $C_{LW} = 0.2$. Thus it is reasonable to expect further reductions in lift-dependent drag for lift coefficients of interest if M_N is reduced to values below 1.2.

6 CONCLUSIONS

A wind-tunnel investigation has been described concerned with the study of flows at supersonic speeds over two highly-swept wings of differing camber but with the same thickness distribution featuring rounded leading-edges. The camber of one wing (A) was derived from that of a wing designed by linear theory while the second (B) was designed using the full-potential method COREL on a 'net wing' basis in the absence of a representation of a body in the method. The main conclusions drawn from the study are as follows:

- (1) The approach to the design of Wing B resulted in an unexpected re-expansion on the upper surface, leading to shocks which were strong enough to separate the boundary layer at a typical supersonic manoeuvre condition.
- (2) Flow separation from the leading edge was avoided on both wings at a typical manoeuvre condition. At low lift, lower-surface separation near the leading edge was absent on Wing B but was indicated on Wing A by a collapse in the lower-surface suction peak.
- (3) For Mach numbers of the local flow-component normal to and just upstream of the upper-surface shock (M_N) greater than 1.3, shock-induced separation was observed. Comparisons between measurement and calculation suggest that such separations on the upper surface induce a loss of lift at a given incidence on the part of the wing inboard of the shock, causing an increase in drag at a given lift.
- (4) The lift-dependent drag of the newly-designed Wing B is lower than that of wing A and further reductions in drag may be achieved in future wing designs by ensuring that M_N is less than 1.2.
- (5) The ARA/BAA multiblock system for solving the Euler equations has been validated for both wings and has been shown to provide a sound basis

for designing wing-body combinations for efficient manoeuvre at supersonic speeds provided account is taken of likely boundary-layer effects.

REFERENCES

- 1 D. S. Miller, E. J. Landrum, J. C. Townsend, W. H. Mason. 'Pressure and force data for a flat wing and a warped conical wing having shockless recompression at Mach 1.62', NASA TP 1759, (1981).
- 2 J. H. B. Smith,. 'Remarks on the structure of conical flow', RAE Technical Report 69119, (1969).
- 3 W. H. Mason, D. S. Miller, J. L. Pittman. 'A supersonic manoeuvre wing design for non-linear attached flow', AIAA Paper No.83-0425, (1983).
- 4 A. Jameson, W. Schmidt, R. Turkel. 'Numerical solutions of the Euler equations by finite volume methods using Runge-Kutta time-stepping schemes', AIAA Paper No.81-1259, (1981).
- 5 N. P. Weatherill, C. R. Forsey. 'Grid generation and flow calculations for aircraft geometries', J. Aircraft, Vol. 22 No.10, (1985), pp 855-860.
- 6 R. M. Wood, S. X. S. Bauer. 'Evaluation of a three-dimensional empirically derived wing at supersonic speeds', AIAA Paper No.88-0481, (1988).
- 7 J. H. B. Smith, J. A. Beasley, D. Short, F. Walkden. 'The calculation of the warp to produce a given load and the pressure due to a given thickness on thin slender wings in supersonic flow', ARC R&M 3471, (1967).
- 8 B. Grossman. 'Numerical procedure for the computation of irrotational flows', AIAA Journal, Vol. 17, No.8, (1979), pp 828-837.
- 9 W. H. Mason, B. S. Rosen. 'The COREL and W12SC3 computer programs for supersonic wing design analysis', NASA CR 3676, (1983).
- 10 P. D. Smith. 'An integral prediction method for three-dimensional turbulent boundary layers', ARC R&M 3738, (1972).
- 11 J. L. Fulker, P. R. Ashill. 'A theoretical and experimental evaluation of a numerical method for calculating supersonic flows over wing-body configurations', to be presented at AGARD FDP Symposium "Validation of Computational Fluid Dynamics", Lisbon, May 2-5 1988.
- 12 L. Gaudet, M. N. Cripps. 'A scheme for a laser-illuminated vapour screen flow visualisation technique for the RAE 8ft x 8ft Wind Tunnel', RAE Technical Memorandum in preparation.
- 13 I. McGregor. 'The vapour screen method of flow visualisation', *Journal of Fluid Mechanics*, Vol. 11, No.4, (1961), pp 481-511.

- 14 H. Liepmann, A. Roshko. 'Elements of gasdynamics' (John Wiley & Sons, 1957).
- 15 R. H. Doe, A. Pagano, T. W. Brown. 'The development of practical Euler methods for aerodynamic design', ICAS 86 5.5, (1986).
- 16 M. J. Siclari. 'The NCOREL computer program for 3D nonlinear supersonic potential flow computations', NASA CR 3694, (1983).
- 17 O. J. Roae, D. S. Miller, J. L. Pittman, P. R. Ashill, J. L. Fulker. 'A full-potential theory analysis of the supersonic aerodynamics of a 60° delta wing-body configuration', AIAA Paper No.88-0480, (1988).
- 18 R. T. Jones, D. Cohen. 'High speed wing theory', (Princeton University Press, 1960).

ACKNOWLEDGMENTS

The efforts of Mrs I. Gaudet in assisting with the analysis and Mr G. L. Riddle in preparing diagrams are gratefully acknowledged.

Fig 1

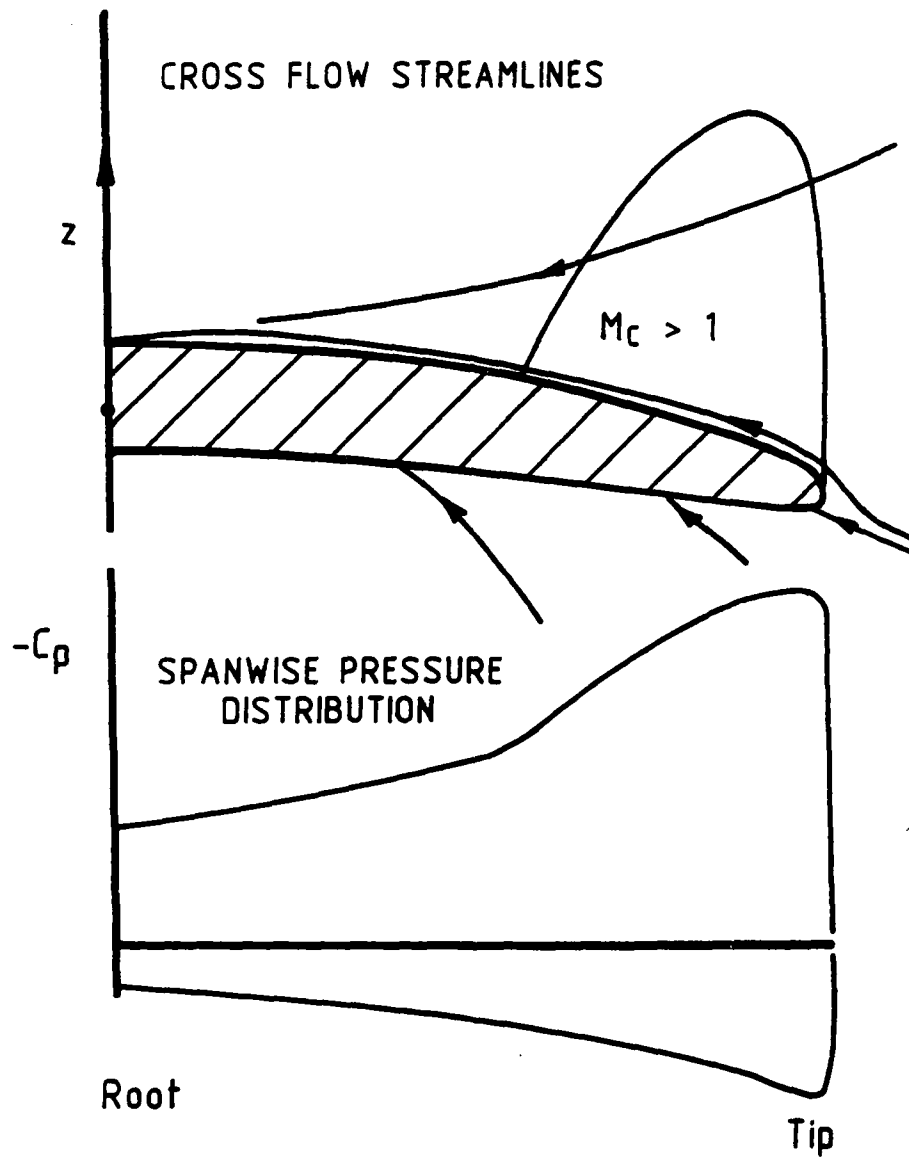


Fig 1 Design for attached flow over a conical wing

Fig 2

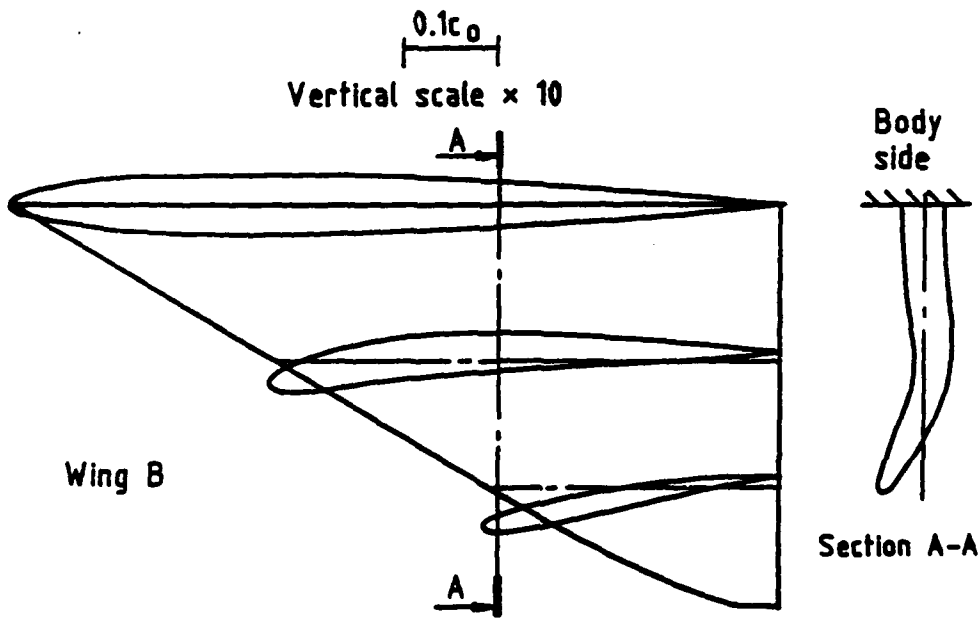
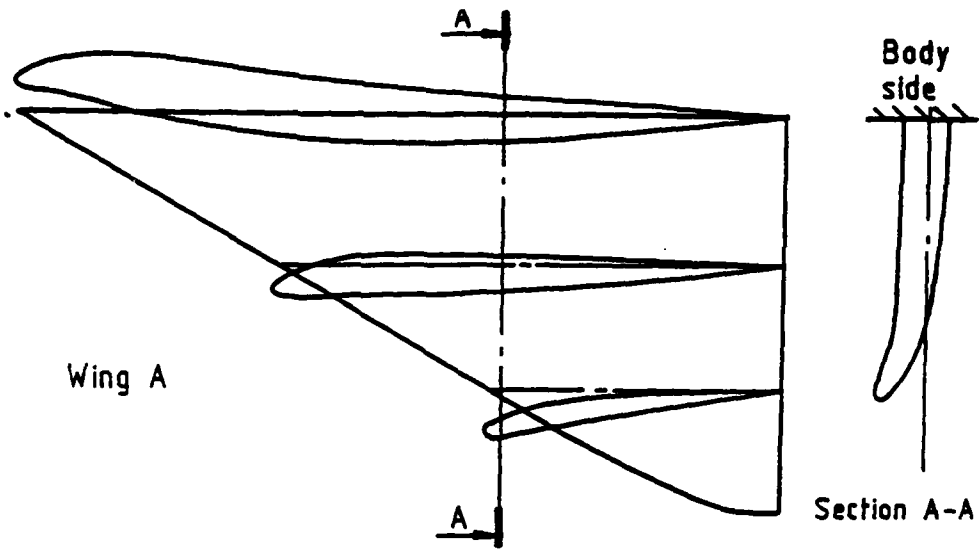


Fig 2 Comparison of typical streamwise and spanwise wing sections for Wings A and B

Fig 3

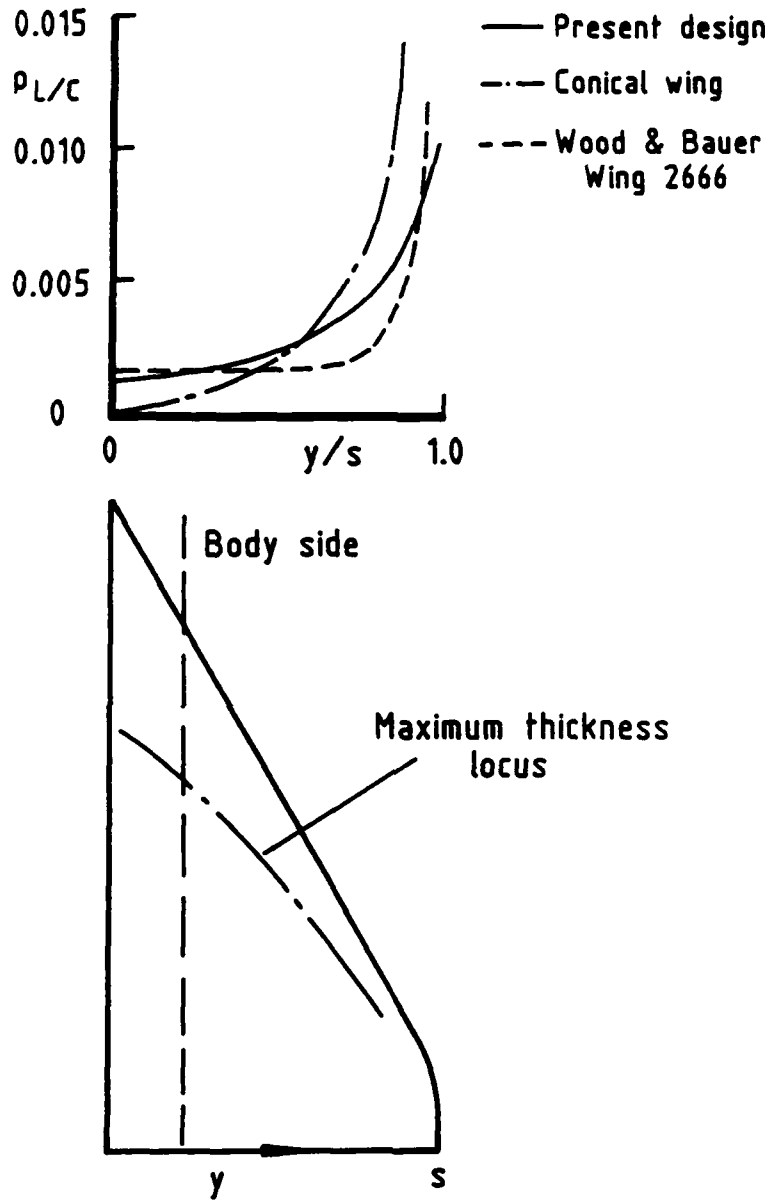


Fig 3 Spanwise distributions of leading-edge radius and maximum thickness locus

Fig 4

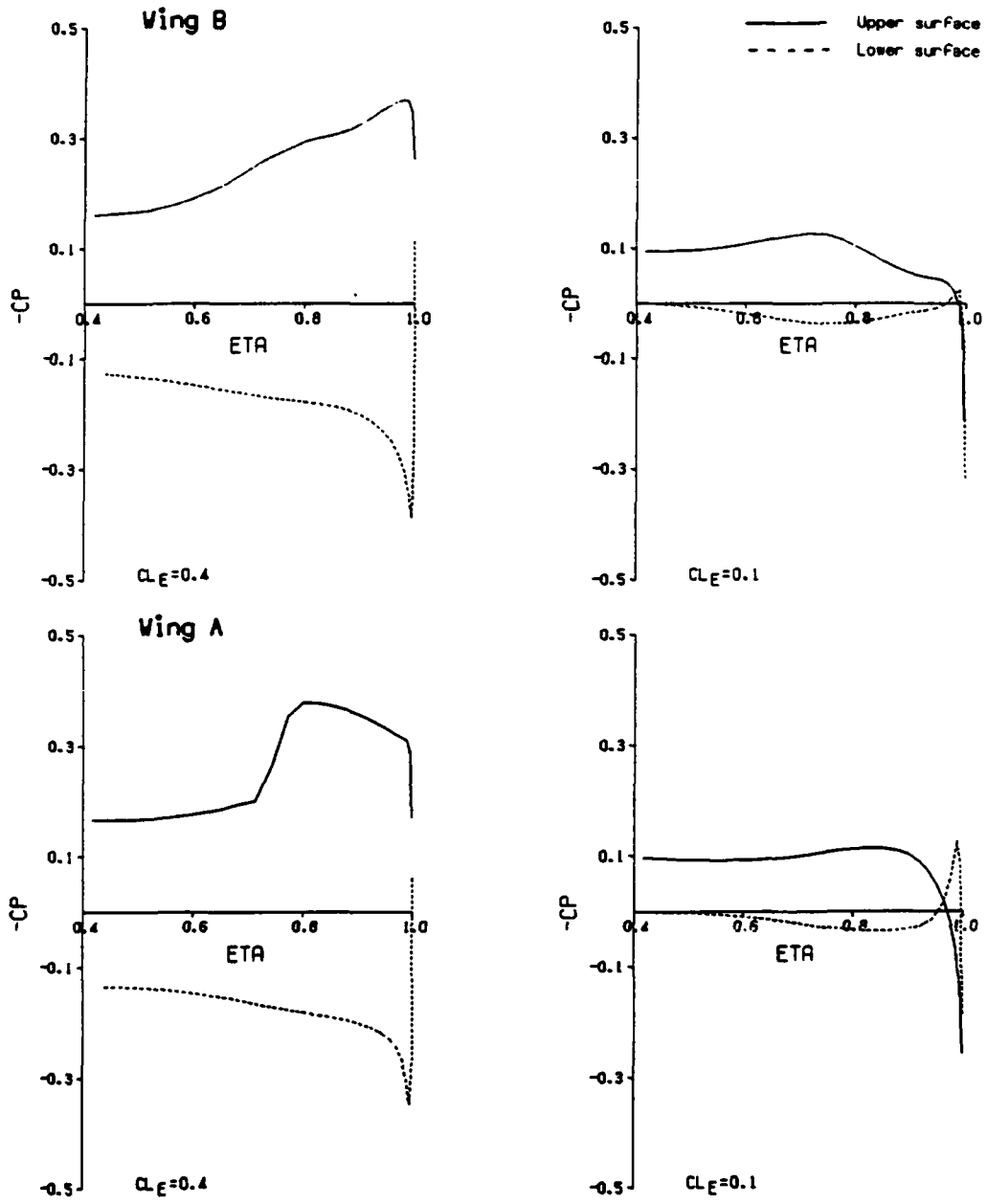


Fig 4 Spanwise pressure distributions, calculated by COREL (net-wing approximation), $M = 1.61$, $X/Co = 0.7051$

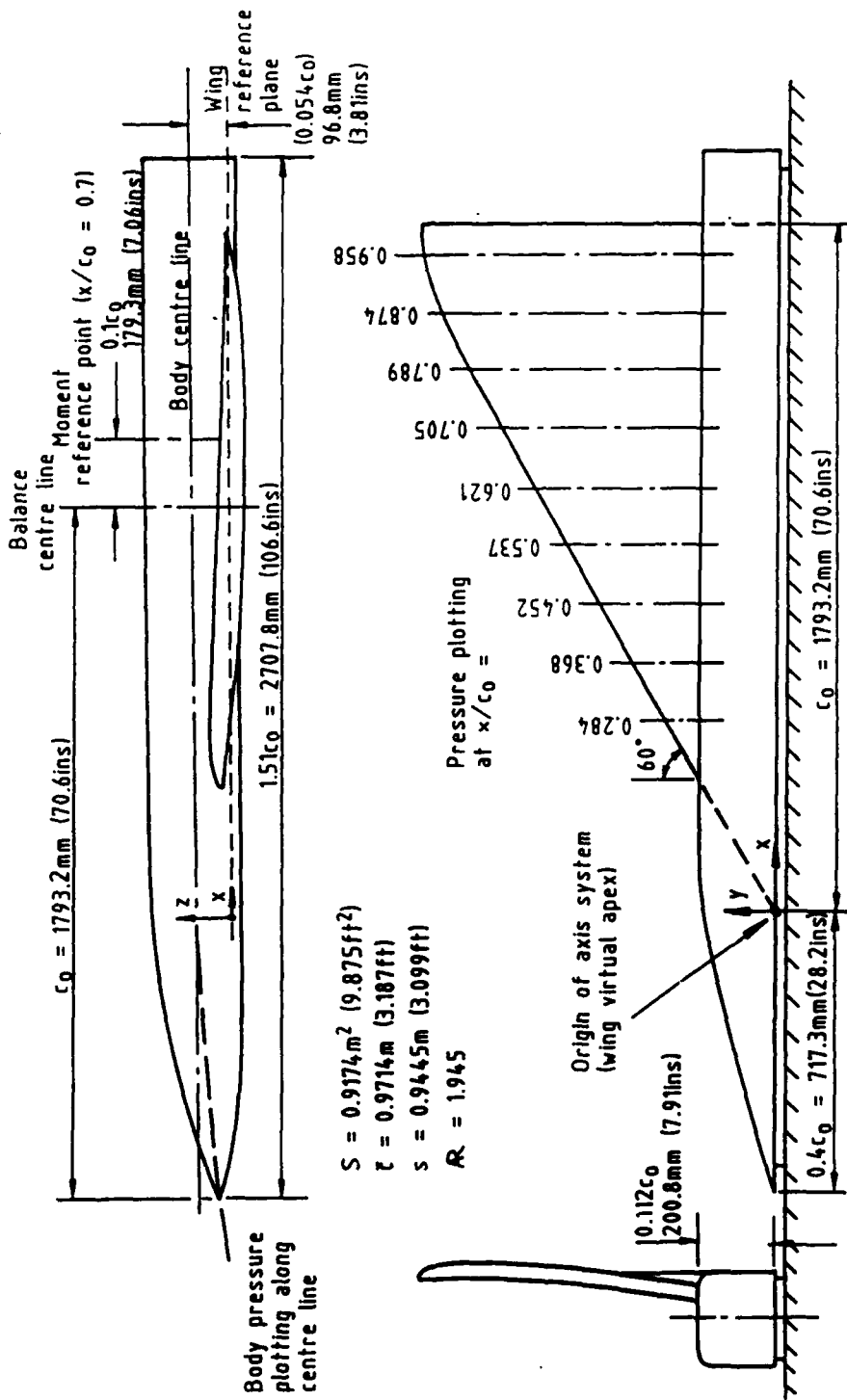


Fig 5 General layout of model showing pressure plotting locations

Fig 6

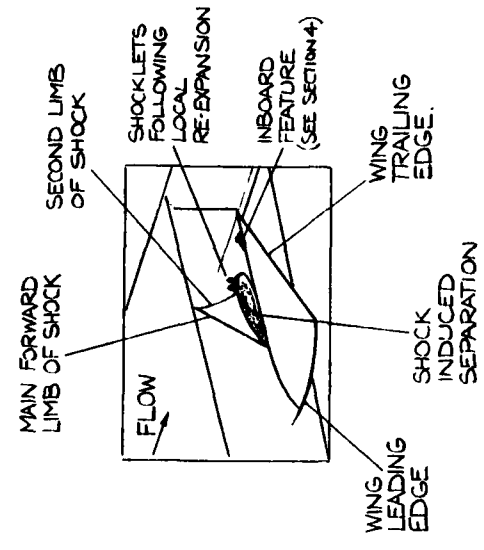


Fig 6 Photograph of laser-illuminated vapour screen, wing A,
 $M = 1.6, C_L = 0.4$

Fig 7

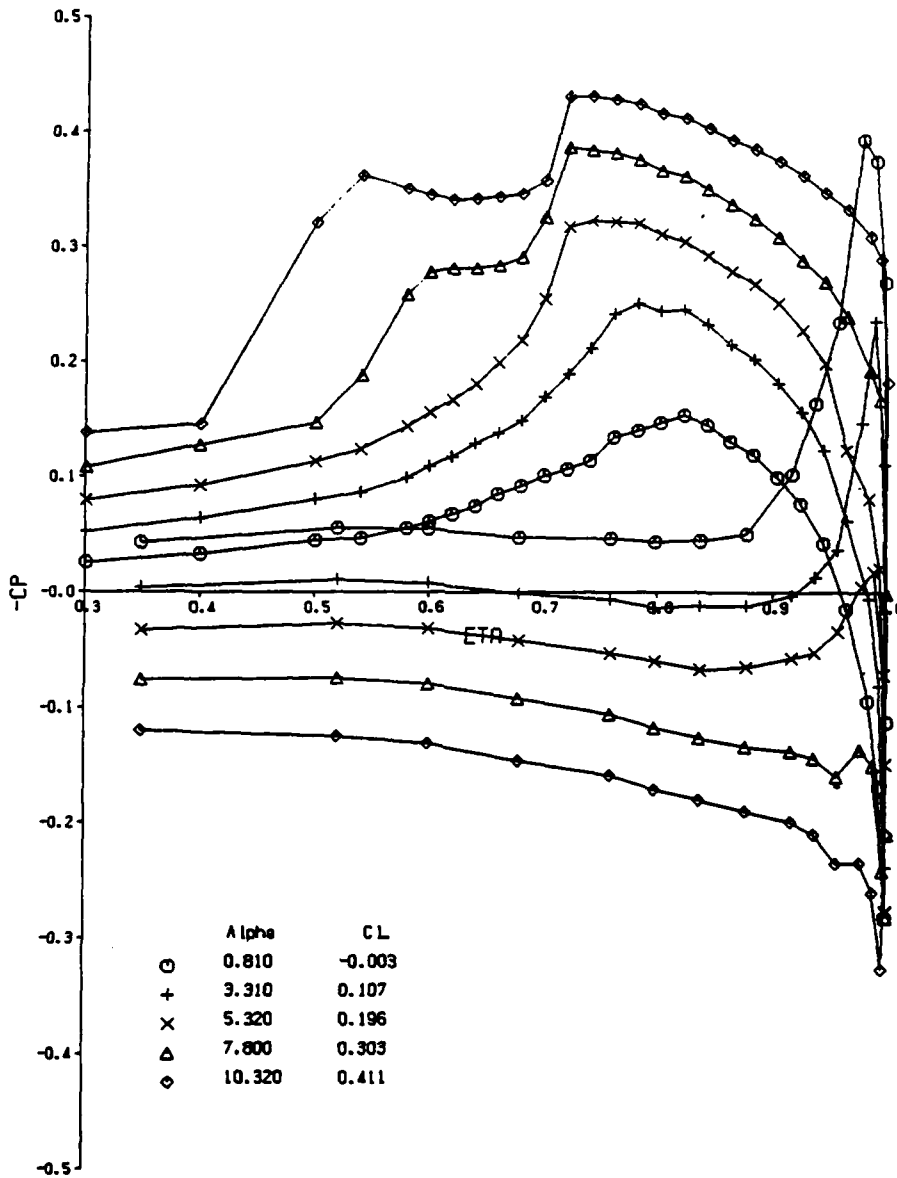
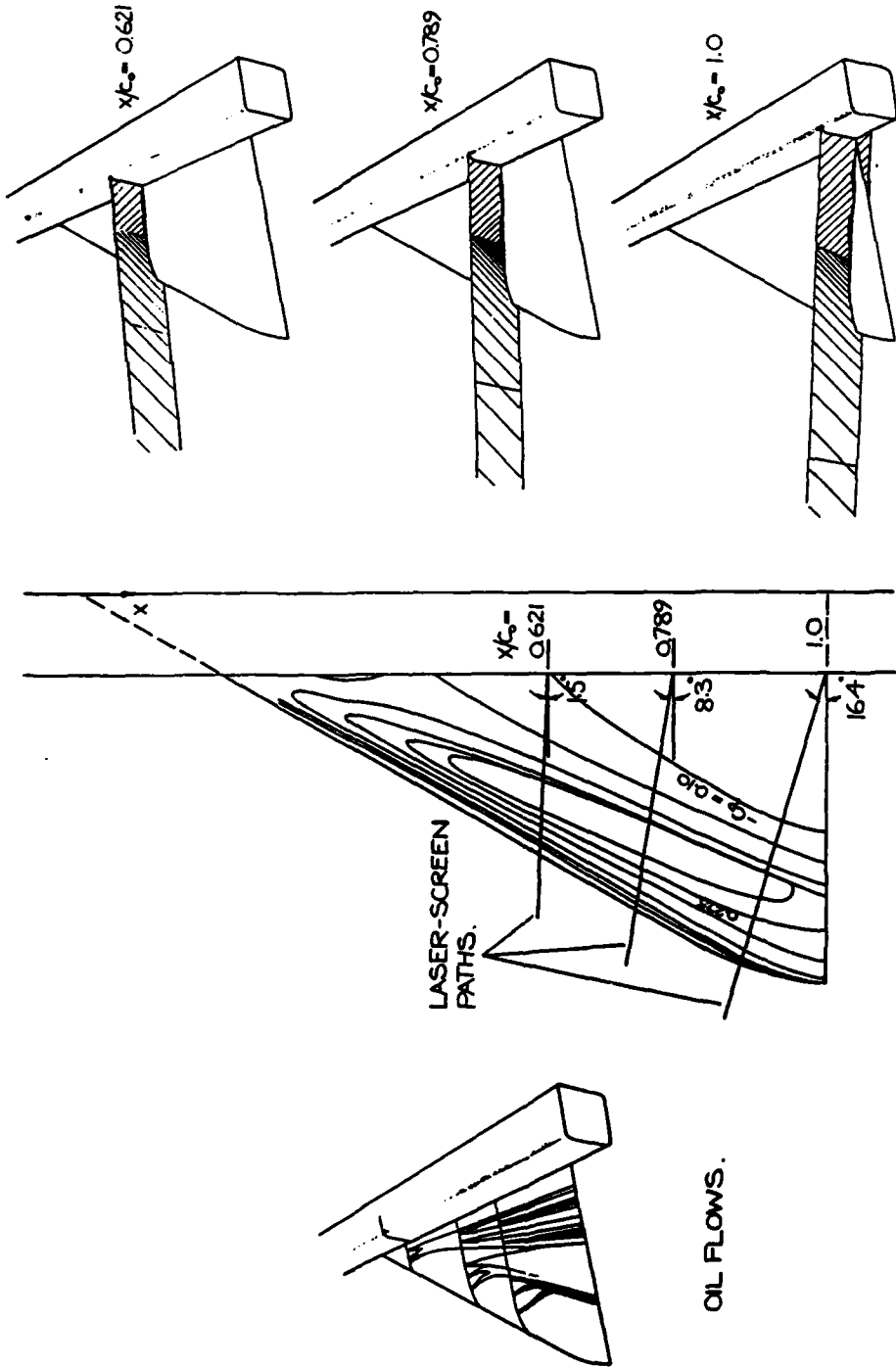


Fig 7 Spanwise pressure distributions Wing A, M = 1.61, X/CO = 0.7051

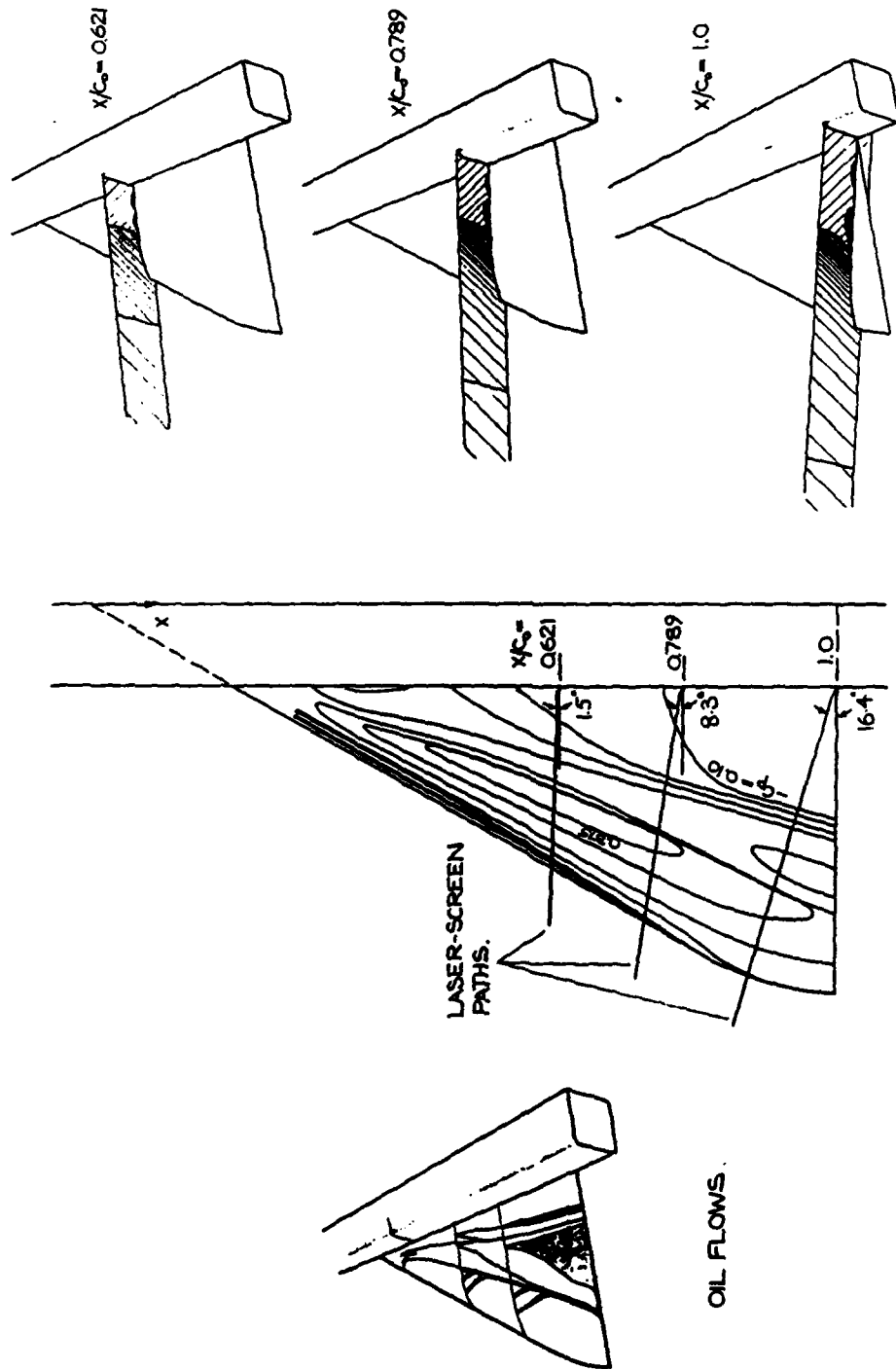
Fig 8



LASER-SCREEN IMAGES.

ISOBARS.

Fig 8 Flow visualisations and upper surface isobars, Wing A, $\alpha = 5.3^\circ$, $CL = 0.2$



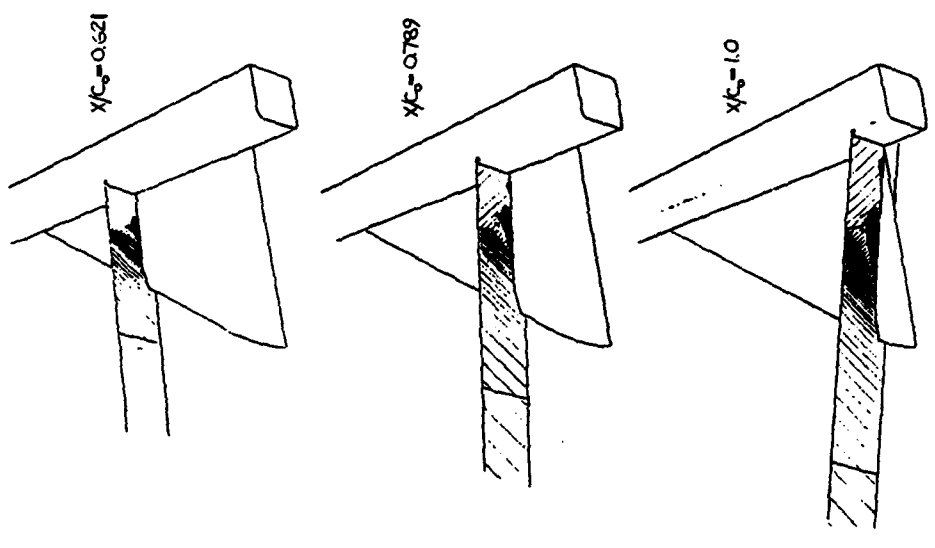
LASER-SCREEN IMAGES.

ISOBARS.

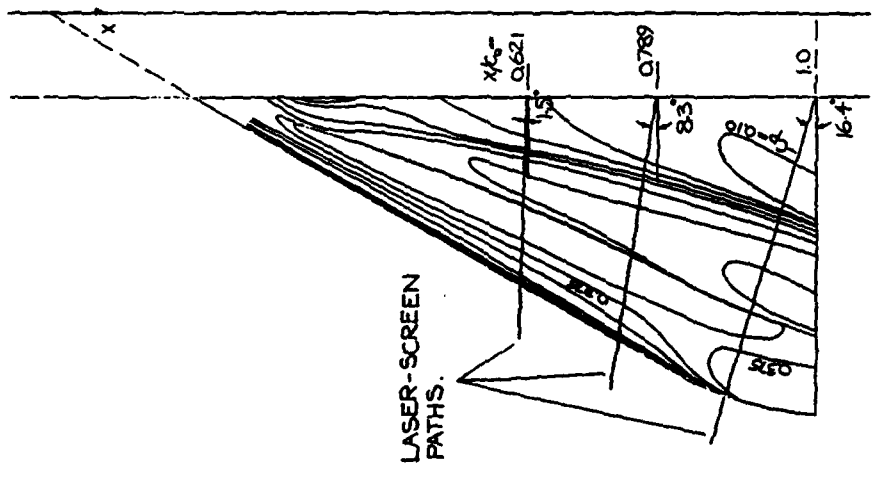
Fig 9 Flow visualisations and upper surface isobars, Wing A, $\alpha = 7.5^\circ$, $CL = 0.3$

Fig 9

Fig 10



LASER-SCREEN IMAGES.



ISOBARS.

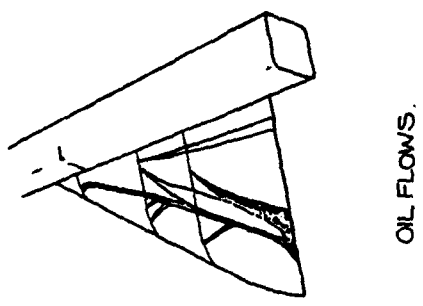


Fig 10 Flow visualisations and upper surface isobars, Wing A, $\alpha = 10^\circ$, $CL = 0.4$

Fig 11

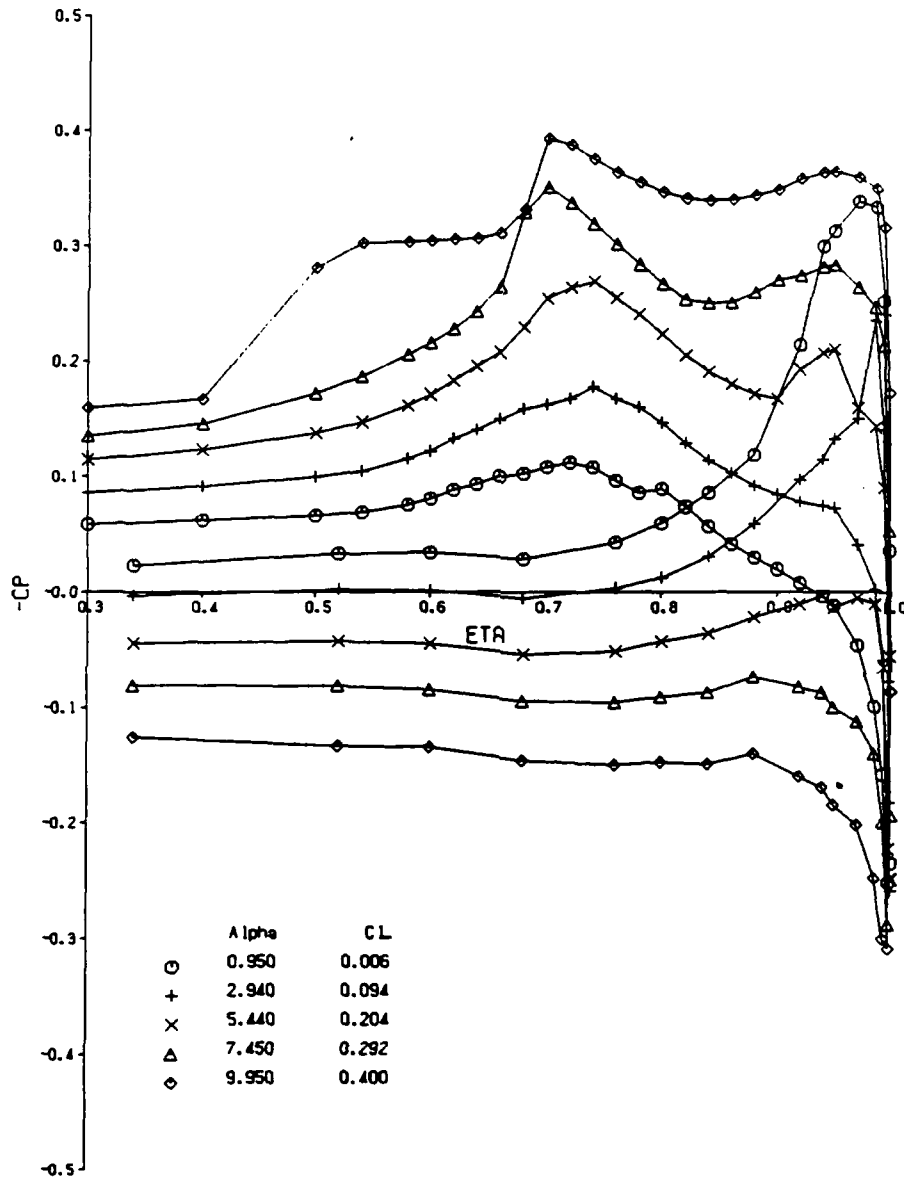


Fig 11 Spanwise pressure distributions Wing B, M = 1.61, X/Co = 0.7051

Fig 12

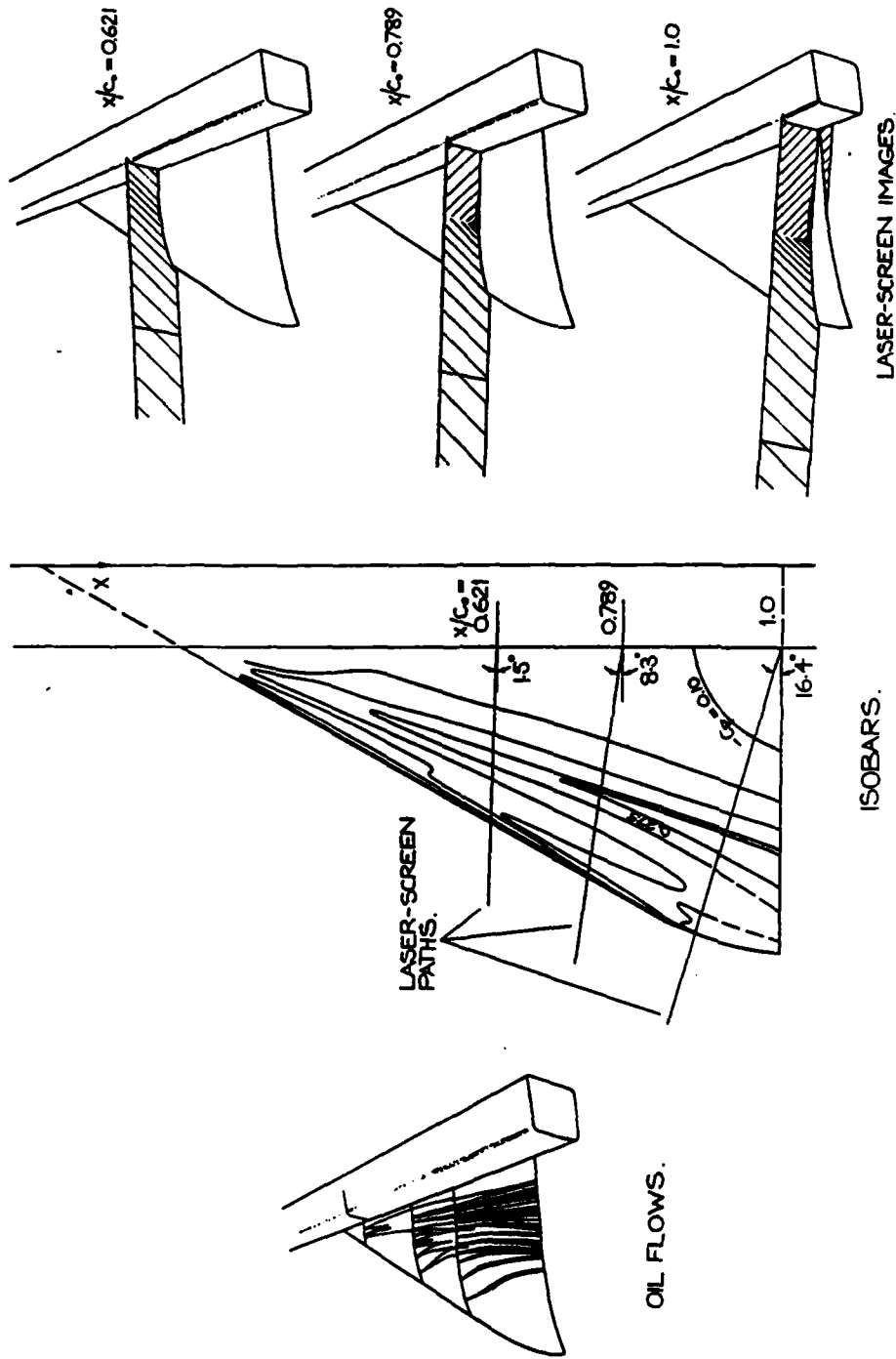


Fig 12 Flow visualisations and upper surface isobars, wing B, $\alpha = 5.4^\circ$, CL = 0.2

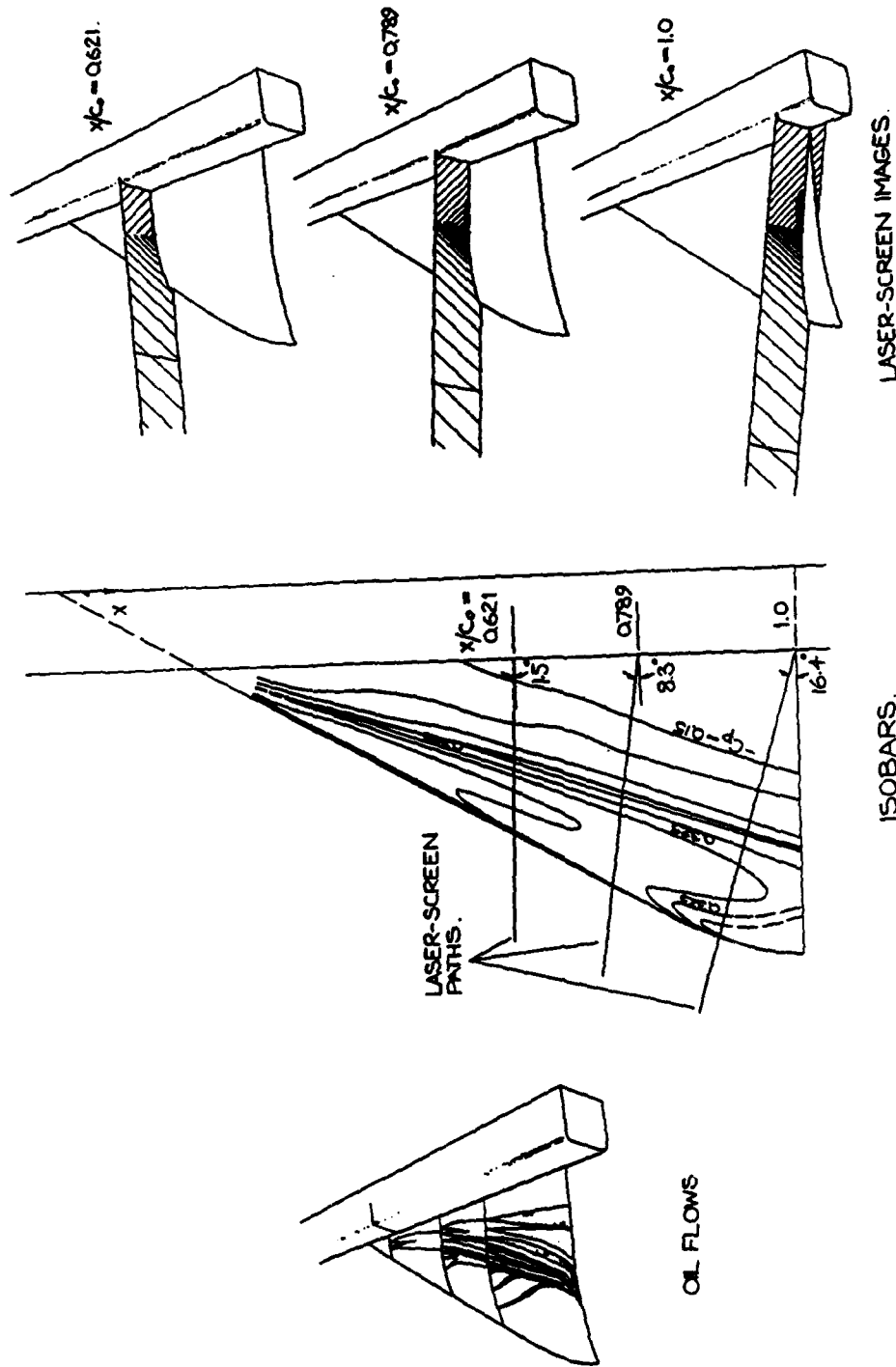


Fig 13

LASER-SCREEN IMAGES.

ISOBARS.

Fig 13 Flow visualisations and upper surface isobars, Wing B, $\alpha = 7.5^\circ$, $CL = 0.3$

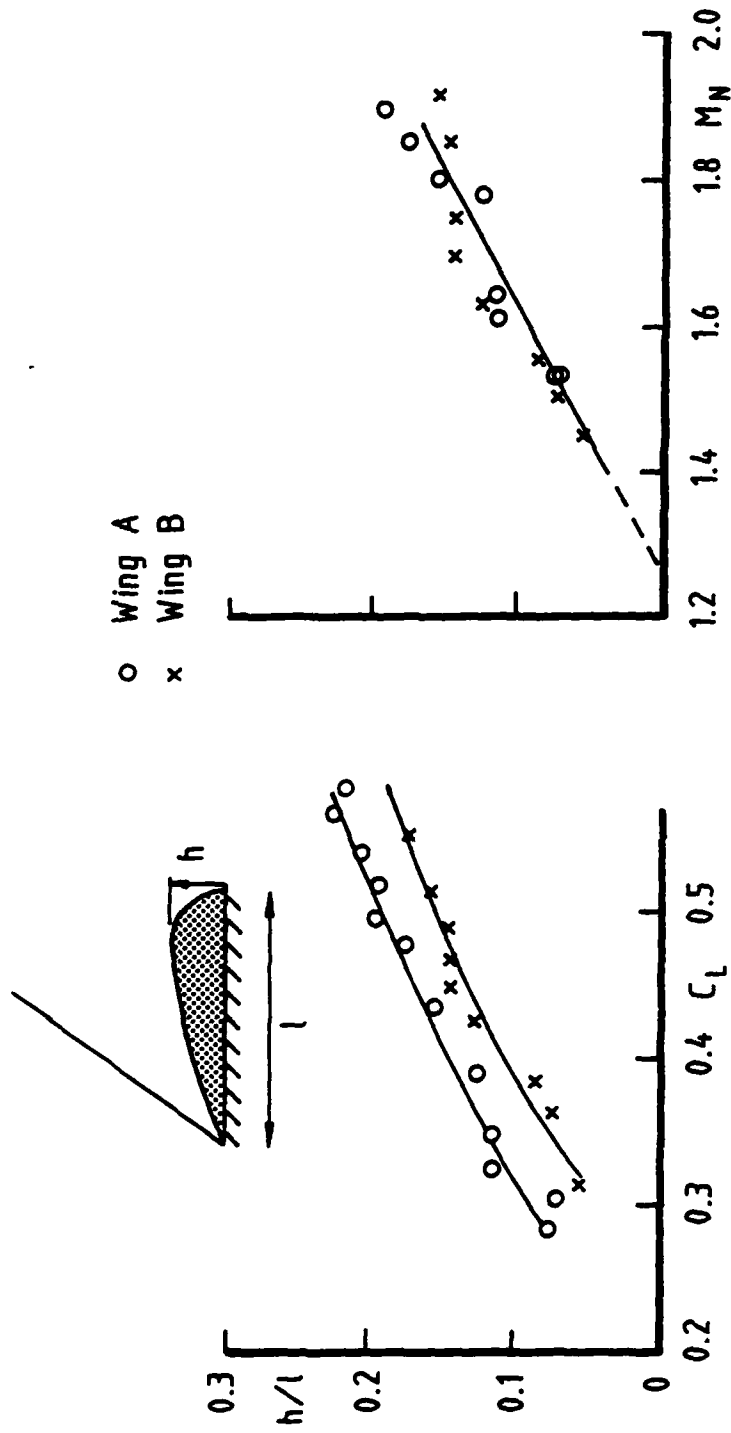


Fig 15

Shock-induced separation bubble bluntness versus lift coefficient and shock upstream Mach number

Fig 16

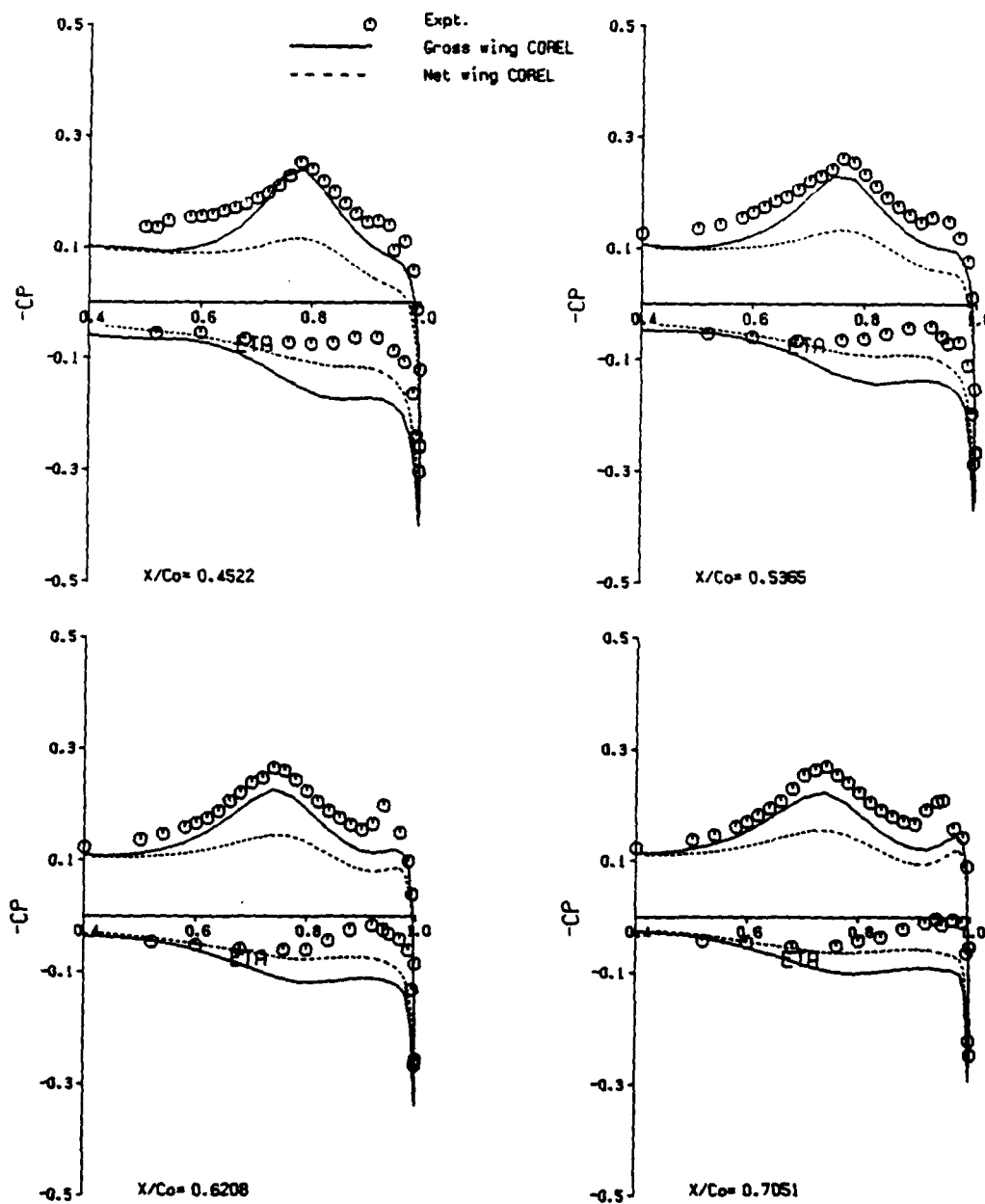


Fig 16 Comparison of spanwise pressure distributions
Wing B, $M = 1.61$, $\alpha = 5.44$

Fig 17

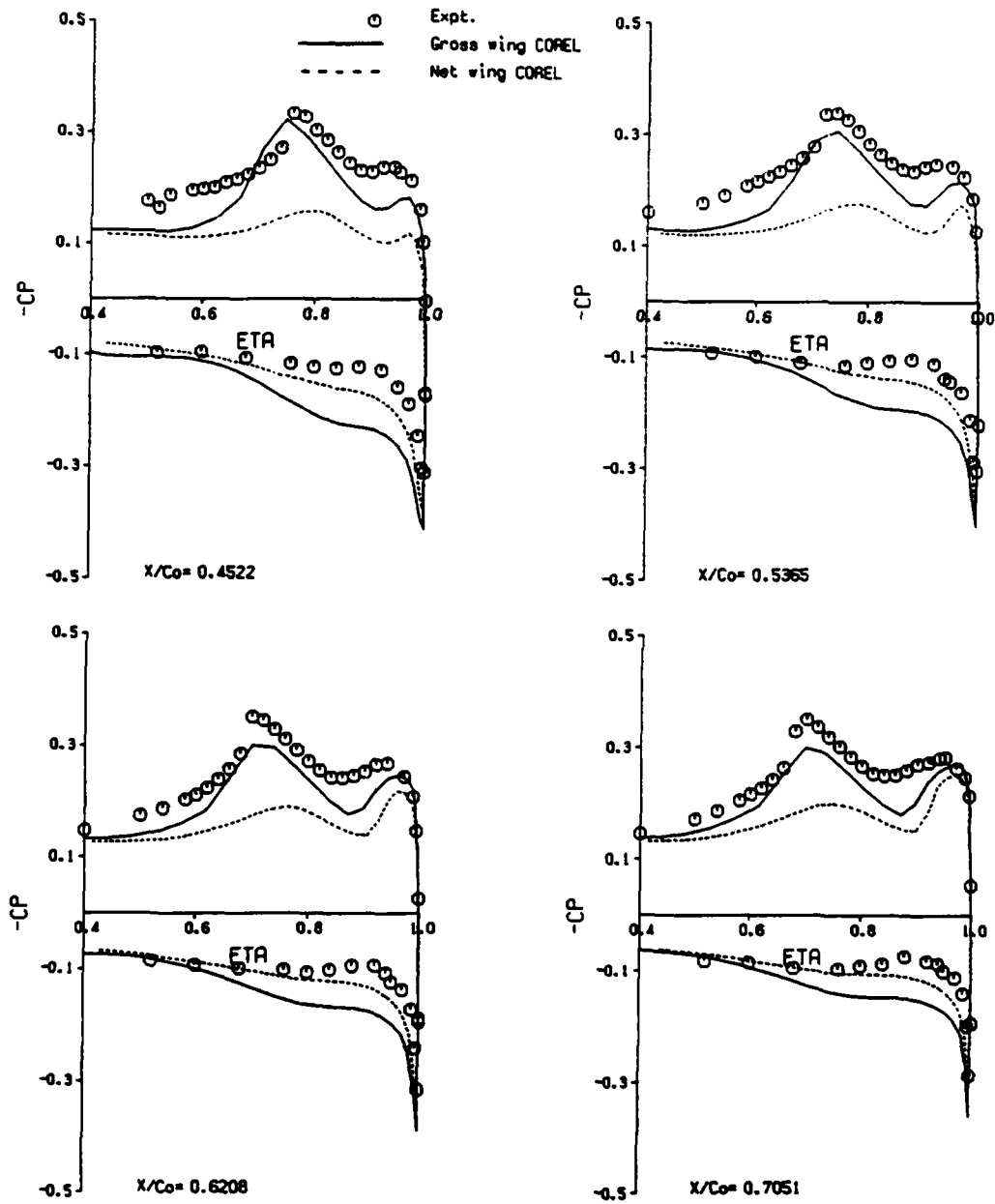


Fig 17 Comparison of spanwise pressure distributions
Wing B, $M = 1.61$, $\alpha = 7.45$

Fig 18a

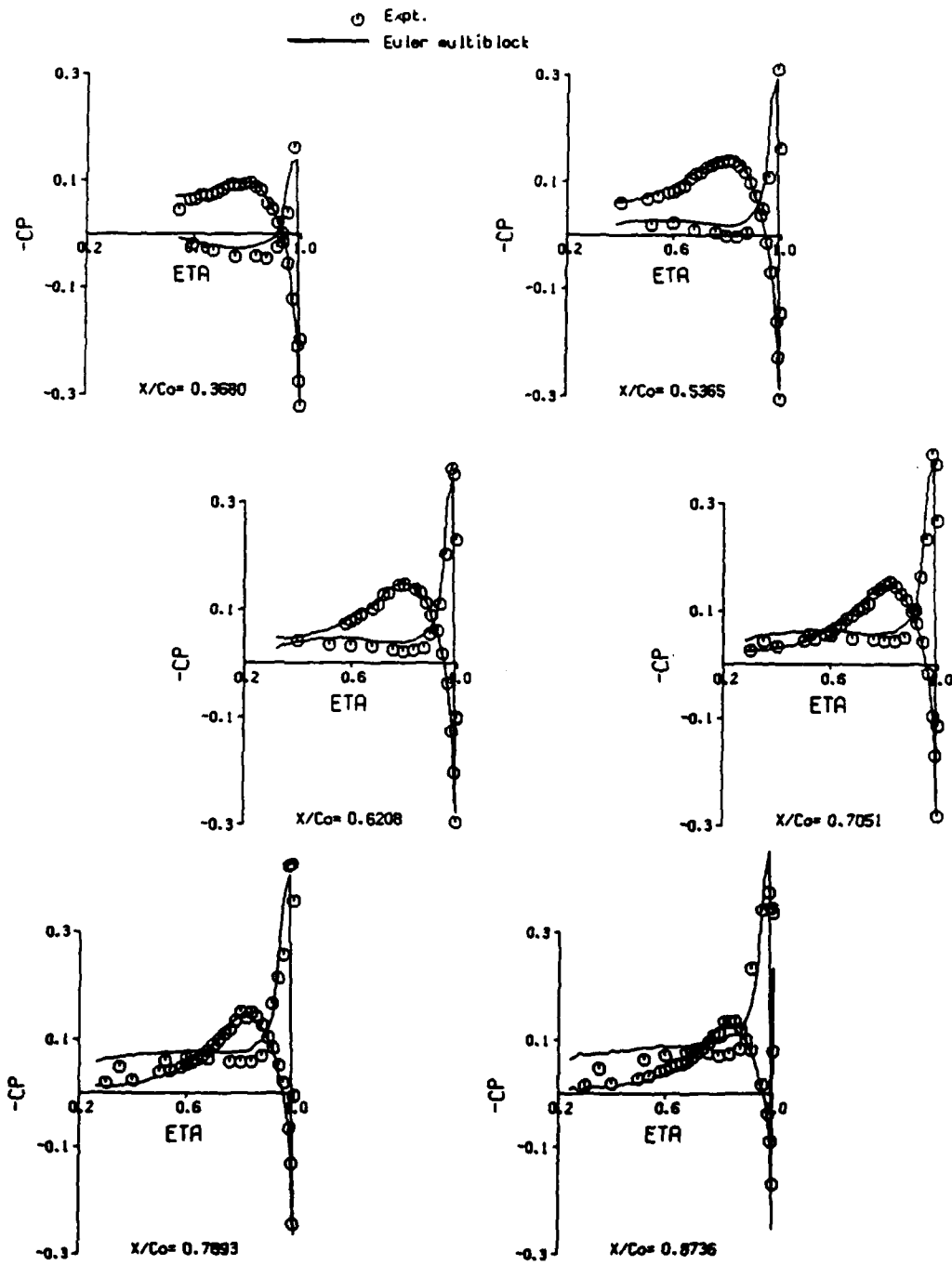


Fig 18a Spanwise pressure distributions Wing A, $M = 1.61$, $CL = 0.0$

Fig 18b

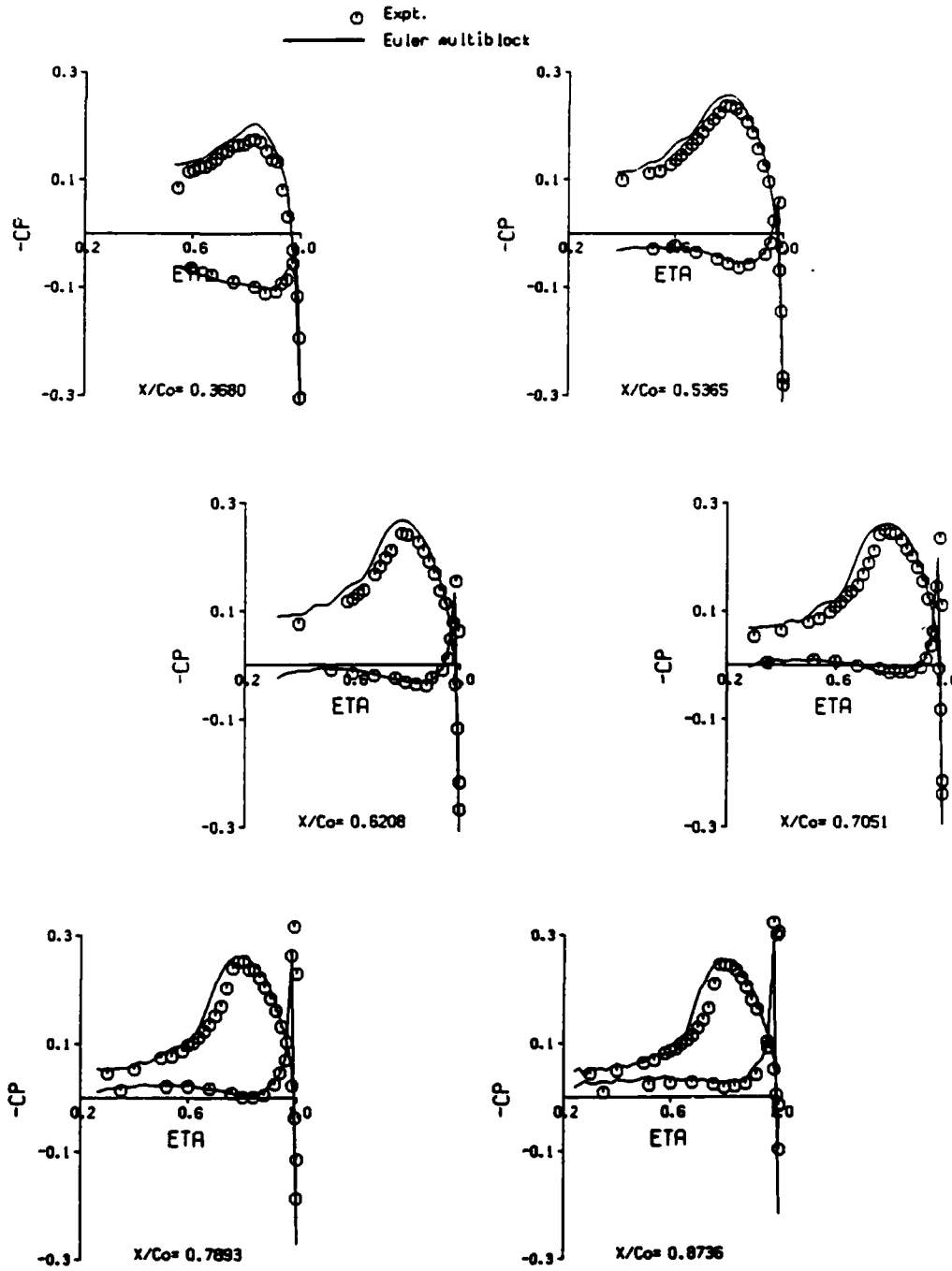


Fig 18b Spanwise pressure distributions Wing A, M = 1.61, CL = 0.1

Fig 18c

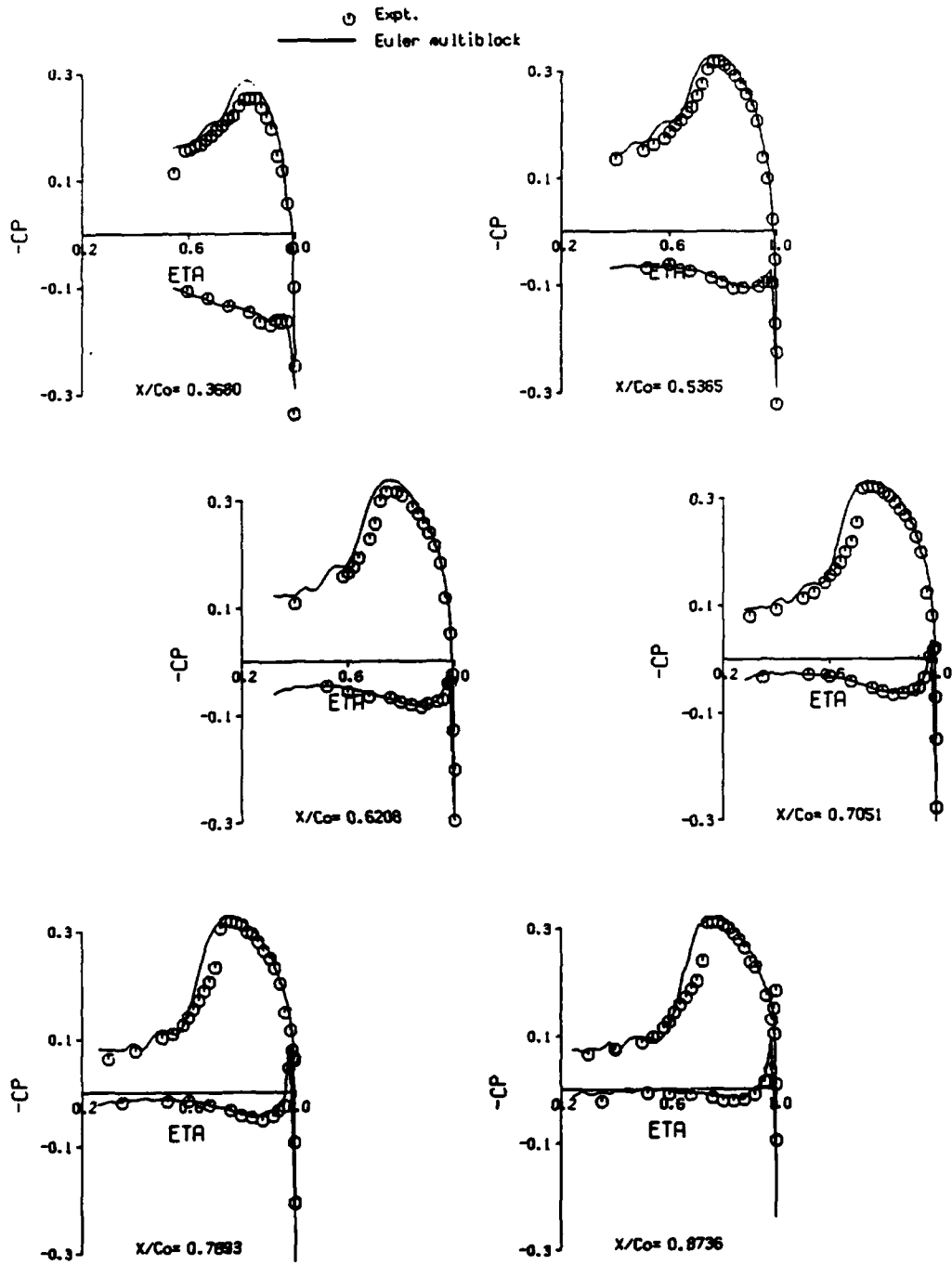


Fig 18c Spanwise pressure distributions Wing A, $M = 1.61$, $CL = 0.2$

Fig 18d

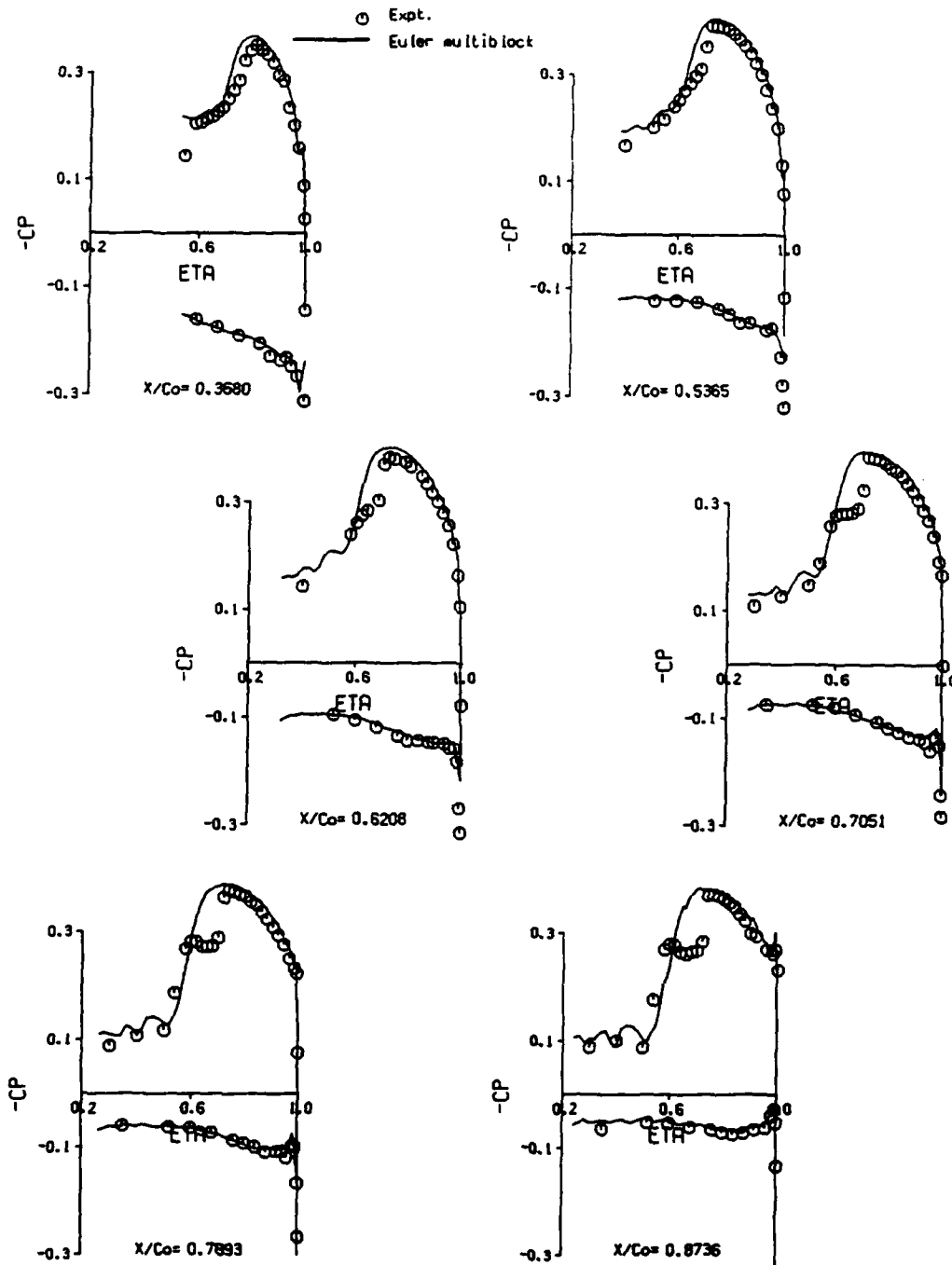


Fig 18d Spanwise pressure distributions Wing A, $M = 1.61$, $CL = 0.3$

TM Aero 2147

Fig 19a

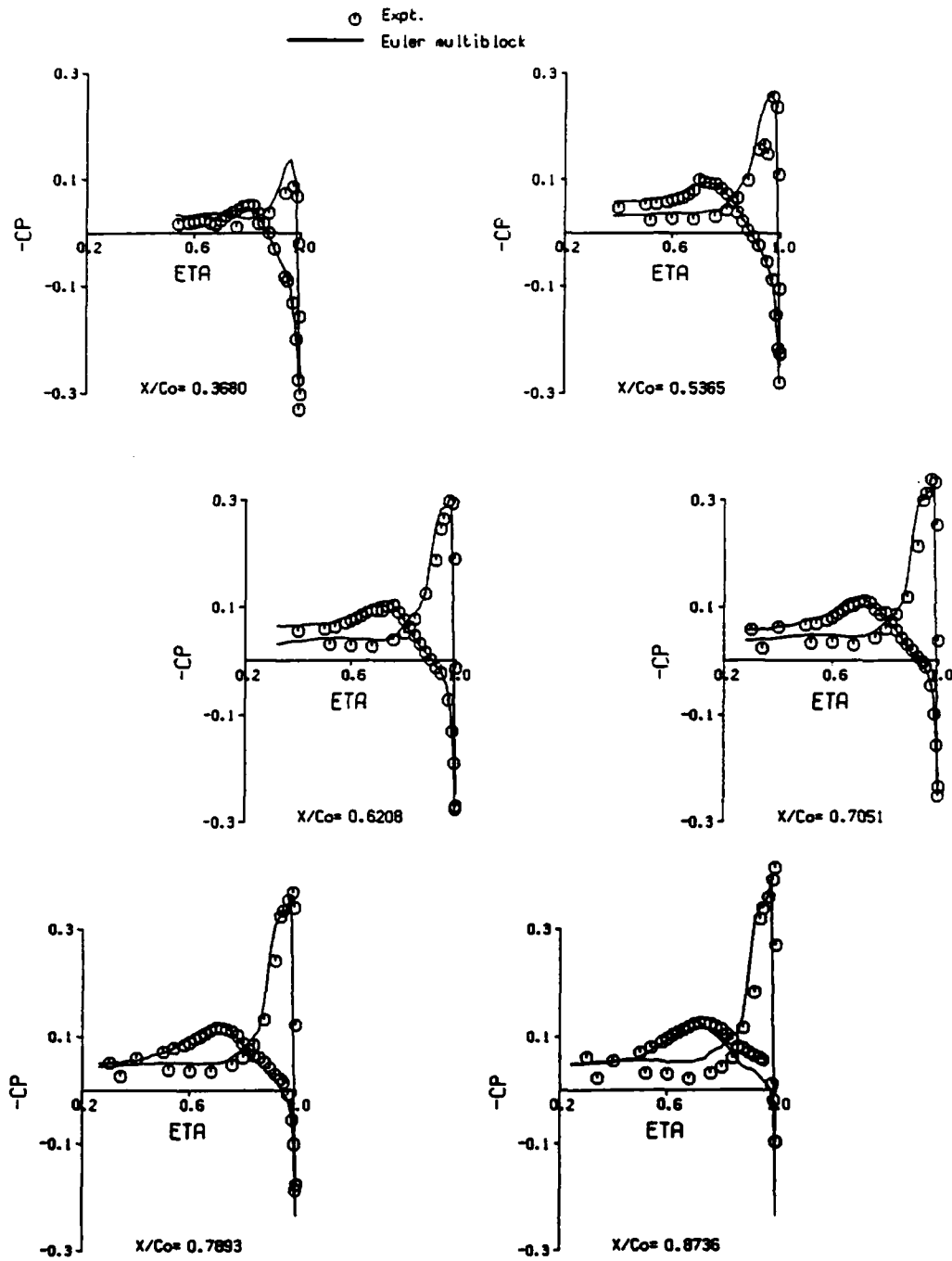


Fig 19a Spanwise pressure distributions Wing B, $M = 1.61$, $CL = 0.0$

Fig 19b

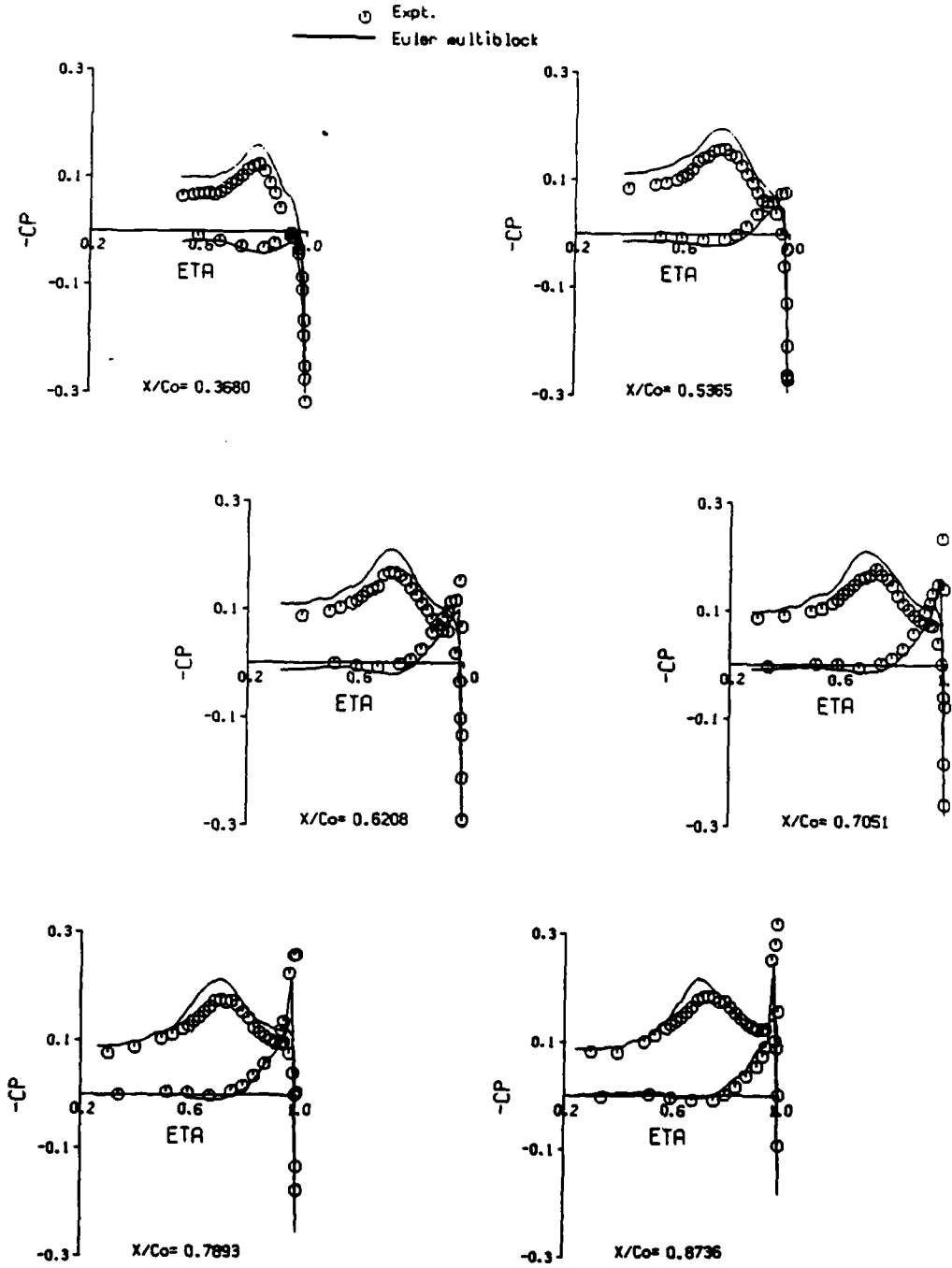


Fig 19b Spanwise pressure distributions Wing B, M = 1.61, CL = 0.1

Fig 19c

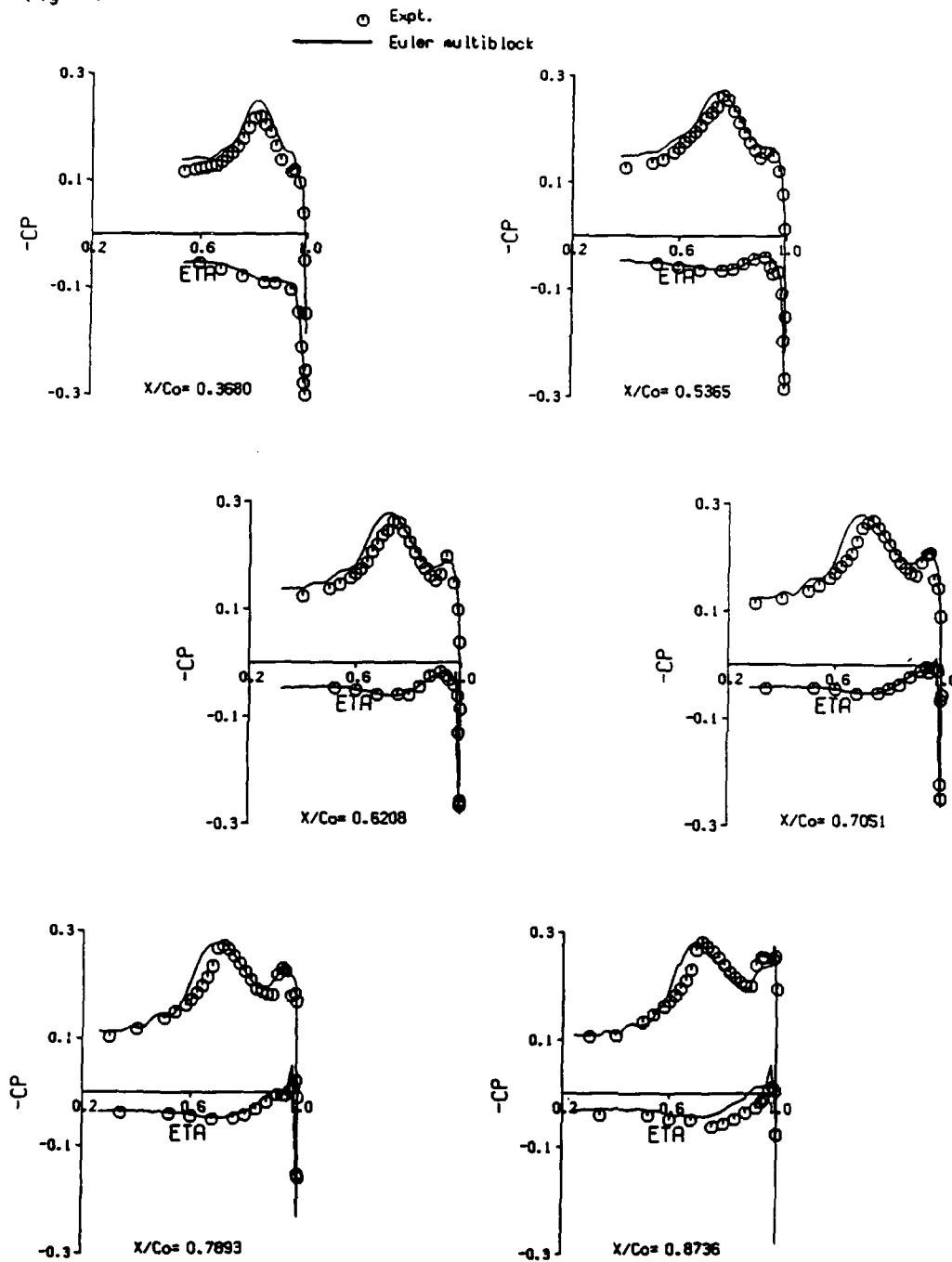


Fig 19c Spanwise pressure distributions Wing B, $M = 1.61$, $CL = 0.2$

Fig 19d

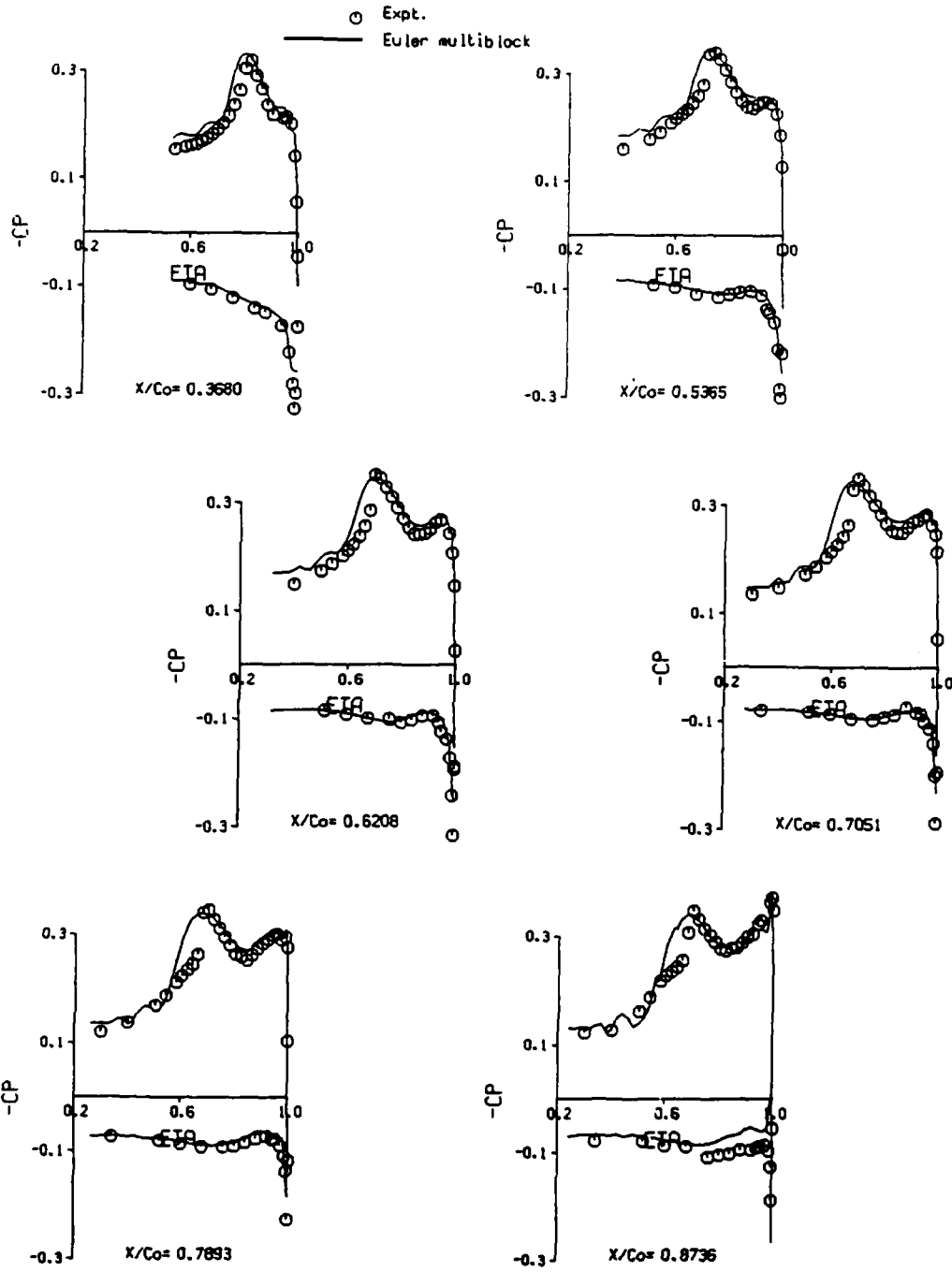


Fig 19d Spanwise pressure distributions Wing B, M = 1.61, CL = 0.3

Fig 20

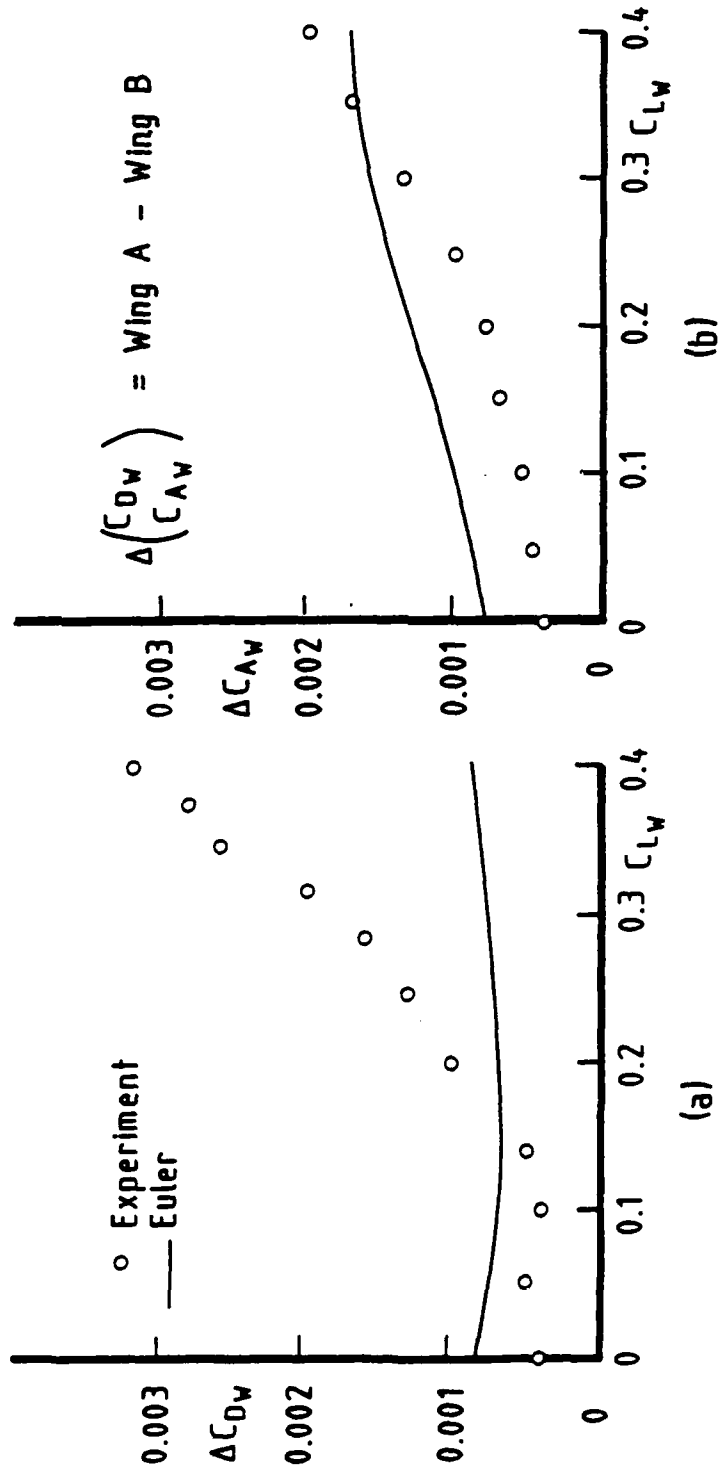


Fig 20 Difference in wing drag and axial force between Wings A and B as predicted and measured, $M_\infty = 1.605$

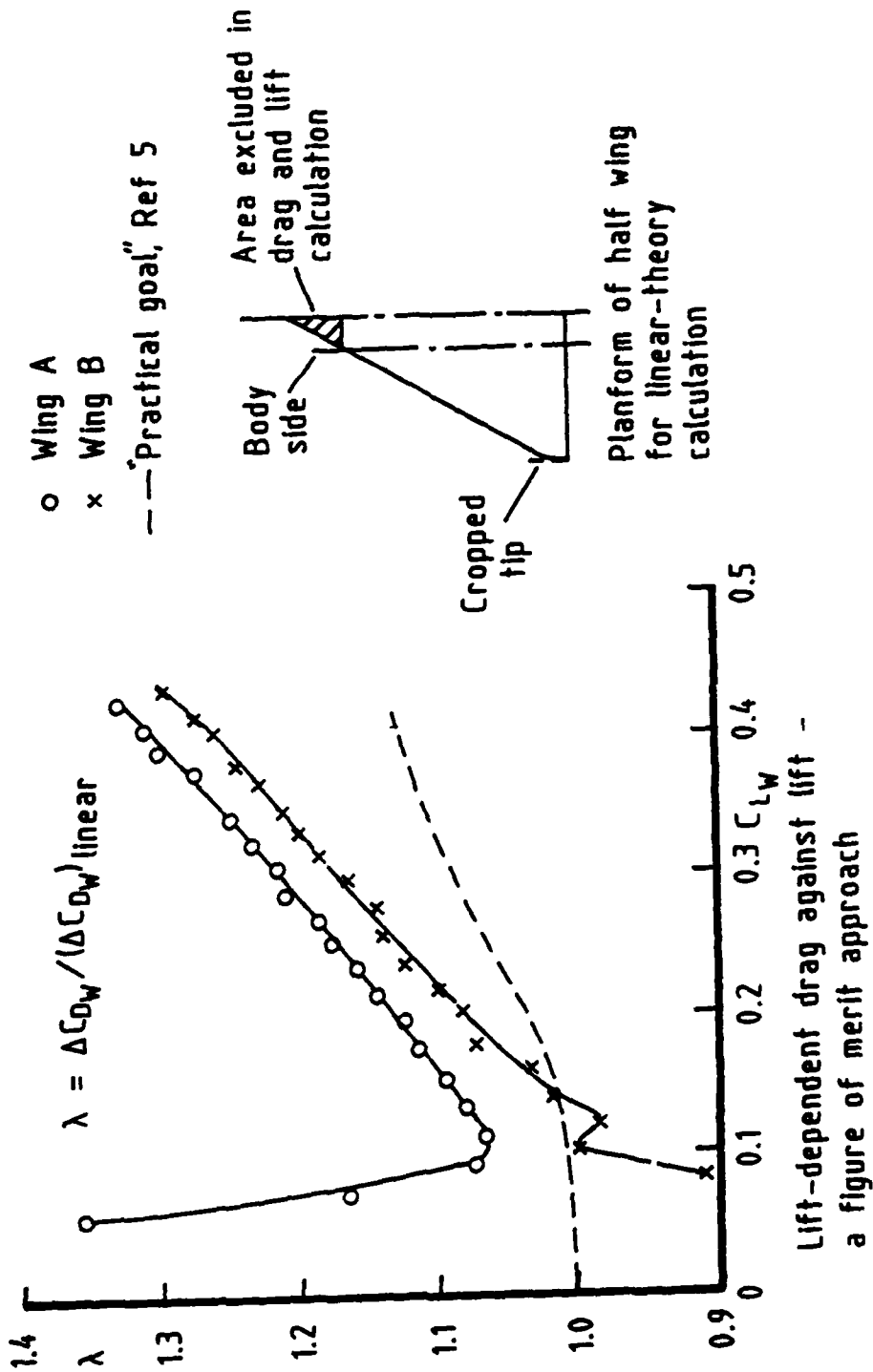


Fig 21

Fig 21 Lift-dependent drag against lift - a figure of merit approach

